INSTITUTO TECNOLÓGICO Y DE ESTUDIOS SUPERIORES DE MONTERREY

Campus Ciudad de México
División de Ingenería y Arquitectura

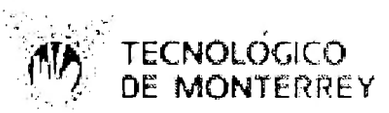

Ingenería Mecatrónica
Departamento de Mecatrónica

"Construction and Calculation of a Darrieus Vertical Axis Wind Turbine with H-Rotor"

Autor:
Distler Johannes 1212107

Profesor: Prof. Dr. Stütz

Asesores: Dr. Ricardo Ganem Corvera
Dr. Jorge Eduardo Brieva Rico

TECNOLÓGICO DE MONTERREY

GEORG-SIMON-OHM HOCHSCHULE NURNBERG

Instituto Tecnológico y de Estudios Superiores de Monterrey

Campus Ciudad de México

División de Ingenería y Arquitectura

"Construction and Calculation of a Darrieus Vertical Axis Wind Turbine with H-Rotor"

Ingenería Mecatrónica

Departamento de Mecatrónica

SS 2008

Autor:

Distler Johannes 1212107

Profesor:	Prof. Dr. Stütz (FH Nuernberg)
Asesores:	Dr. Ricardo Ganem Corvera
	Dr. Jorge Eduardo Brieva Rico

Abstract

Since ancient times humans have attempted to harness the wind energy through diversified means, vertical axis wind turbines (VAWTs) have been one of the most important pieces of equipment to achieve this. The purpose of this work is to calculate and construct a small-size Darrieus H-Rotor, so to be able to construct the turbine one day. An H-Rotor has a simple construction, however the calculation is complicated because the aerodynamic analysis is quite complex. Furthermore there are some opportunities to test the performance of the rotor this is also included in this thesis.

The difficulty is that there has not been many investigations nor much researches in this area of wind energy. Because of this, it isn't easy to gather important information because the technology of Darrieus type turbines is relatively new.

Table of contents

Table of figures 5

Abbreviations and Acronyms 7

1.0 Introduction 9
- 1.1 Wind energy 9
- 1.2 History of wind power 10
- 1.3 History of VAWT´s and HAWT´s 12
- 1.4 Comparative study between VAWT and HAWT 14
- 1.5 Current situation of wind power 17

2.0 Theoretical background 19
- 2.1 Betz criteria 19
- 2.2 TIP speed ratio 20
- 2.3 Lift and drag definition 21
- 2.4 Airfoil shape and lift/drag coefficient 24

3.0 Calculation 27
- 3.1 General mathematical expression for aerodynamic analysis 27
  - 3.1.1 Power available from the wind 27
  - 3.1.2 Variation of local angle of attack 29
  - 3.1.3 Variation of local relative flow velocity 29
  - 3.1.4 Variation of tangential and normal forces 30
  - 3.1.5 Calculation of total torque 30
  - 3.1.6 Power output 31
- 3.2 Definition of V_a 31
  - 3.2.1 Momentum model 31
  - 3.2.2 Single streamtube model 32
  - 3.2.3 Determination of V_a 33
- 3.3 Relation between α and θ 34
- 3.4 Solution of the calculation 38

3.4.1 Investigation of the equations of C_l and C_d with EES 41
3.4.2 Determination of the values R, l, S and f 43
3.4.3 Torque and power calculation 45
3.4.4 Torque/power with different TSR 45

4.0 Construction process 48
4.1 Determinations for the stress calculations 48
4.2 Part 1 50
4.2.1 Airfoil 50
4.2.2 Support arms 52
4.2.3 Turning platform 54
4.3 Part 2 55
4.3.1 Generator System 55
4.3.2 Shaft 57
4.3.3 Parallel key 58
4.3.4 Bearing 59
4.3.5 Support structure 60
4.4 Entire assembly 61

5.0 Performance testing 64
5.1 Introduction – multiple fans test 64
5.2 Setting up the rotor, the fans and the equipment 65
5.3 Band brake testing method 65
5.4 Inertia acceleration testing method 67

6.0 Conclusion 68

Appendix 69

References 79

Poster 81

Table of figures

Figure 1:	Weibull distribution	9
Figure 2:	Wind speed and height	9
Figure 3:	Old HAWT	10
Figure 4:	Types of VAWT	12
Figure 5:	Modern VAWT	14
Figure 6:	Power curve of different turbines	16
Figure 7:	Wind power capacity worldwide 1997-2010	17
Figure 8:	Primary energy distribution, 2007	18
Figure 9:	Schematic of fluid flow through an actuator	19
Figure 10:	The Betz criteria P/P_0 as a function of V_2/V_1	19
Figure 11:	Airflow around an airfoil	21
Figure 12:	Forces acting on an airfoil	22
Figure 13:	Airfoil simulation program DesignFOIL	24
Figure 14:	Virtual wind tunnel results	25
Figure 15:	C_l vs. angle of attack	26
Figure 16:	C_d vs. angle of attack	26
Figure 17:	Flow velocities of straight-bladed Darrieus-type VAWT	28
Figure 18:	Force diagram of a blade airfoil	29
Figure 19:	Schematic of single streamtube model	32
Figure 20:	Investigation of V_a with the betz criteria	33
Figure 21:	H-Rotor model	34
Figure 22:	Angle of attack α vs. θ, TSR= 0.5	36
Figure 23:	Angle of attack α vs. θ, TSR= 1	36
Figure 24:	Angle of attack α vs. θ, TSR of 2, 3, 4 and 5	37
Figure 25:	Software EES	38
Figure 26:	Comparison of lift coefficient C_l	39
Figure 27:	Comparison of drag coefficient C_d	40
Figure 28:	Diagram of C_p vs. TSR for various solidity	41
Figure 29:	Torque of the three blades	43
Figure 30:	Calculated total power of the H-Rotor	44
Figure 31:	Diagram of the torque of one blade with different TSR	45
Figure 32:	Diagram of the total power with different TSR	46
Figure 33:	Profile of a NACA 63-018 airfoil	50

Figure 34:	Construction of the airfoil profile in ProE	50
Figure 35:	Front view of the airfoil	51
Figure 36:	Back view of the airfoil	51
Figure 37:	Aluminium support arm	52
Figure 38:	Assembly of blade and support arm	52
Figure 39:	Blade with fixed support arms	52
Figure 40:	Fixation of the support arms on the two discs	54
Figure 41:	Assembled part 1	54
Figure 42:	The lower disc of the turning table	54
Figure 43:	Simplified view in ProEngineering	56
Figure 44:	Connection point to the turning platform with threaded hole	57
Figure 45:	Connection point to the generator	57
Figure 46:	Assembly of hollow shaft, generator shaft and parallel key	59
Figure 47:	Assembled flanged bearing	59
Figure 48:	Exploded support structure of part 2	60
Figure 49:	Mounting plate with 4 welded bars	60
Figure 50:	Assembly of part 1 and 2 with threaded pin	61
Figure 51:	Assembly of the Darrieus H-Rotor	63
Figure 52:	Band brake system	66

Abbreviations and Acronyms

A	projected frontal area of turbine
AC	alternating current
AOA	angle of attack
C_d	drag coefficient
C_l	lift coefficient
C_n	normal force coefficient
C_p	turbine overall power coefficient
C_t	tangential force coefficient
D	blade drag force
DC	direct current
D_a	outer diameter
D_i	inside diameter
d	shaft diameter
$F_{1/2}$	single force of the pin
F_n	normal force
F_t	tangential force
F_{ta}	average tangential force
f	blade chord length
HAWT	horizontal axis wind turbine
h	thickness of the airfoil
L	lift force
l	length of the blade
l_s	length of the shaft
N	number of blades
NACA	National Advisory Committee of Aeronautics
P	total power}
PM	permanent magnet
ProE	Pro Engineering Wildfire
P_a	power available in the wind
P_{max}	maximum possible power
p_m	medial surface pressure
Q	total torque

$Q_{1/2}$	single torque of the pin
Q'	maximum torque for one support arm
Q_{max}	maximum torque
Q_{min}	minimum torque
R	maximum rotor radius
RPM	Revolutions Per Minute
S	solidity
TSR	tip speed ratio
VAWT	vertical axis wind turbine
V_2	wake velocity in downstream side
V_a	induced velocity
V_c	chordal velocity component
V_n	normal velocity component
V_t	tangential velocity
V_w	wind velocity
W	relative flow velocity
W_z	resisting moment z-axis
$x_{1/2}$	lever of the pin
α	angle of attack
γ	blade pitch angle
θ	azimuth angle
λ	tip speed ratio
λ_{min}	minimum tip speed ratio
ρ	air density
σ_{bmax}	maximum bending load
σ_{bzul}	allowed bending load
τ_{smax}	maximum shearing strain
τ_{tschN}	allowed shearing strain
ω	angular velocity of turbine
ω_{max}	maximum angular velocity
ω_{min}	minimum angular velocity

1.0 Introduction

1.1 Wind energy

The Sun heats our atmosphere unevenly, so some patches become warmer than others. These warm patches of air rise, other air blows in to replace them - and we feel a wind blowing. Wind energy is the kinetic energy that is present in moving air. The amount of potential energy depends mainly on wind speed, which is of course not constant, shown in the Weibull distribution (figure 1). That plot shows the modal wind speed of 5.5 m/s, which is the speed of the most frequent occurrence.

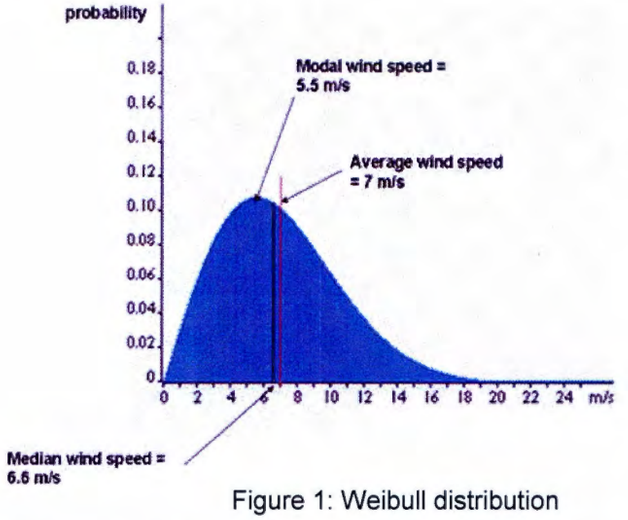

Figure 1: Weibull distribution

It is also affected slightly by the density of the air, which is determined by the air temperature, barometric pressure, and altitude (Figure 2). For any wind turbine, the power and energy output increases dramatically as the wind speed increases. Therefore, the most cost-effective wind turbines are located in the windiest areas. Wind speed is affected by the local terrain and increases with height above the ground, so wind turbines are usually mounted on tall towers.

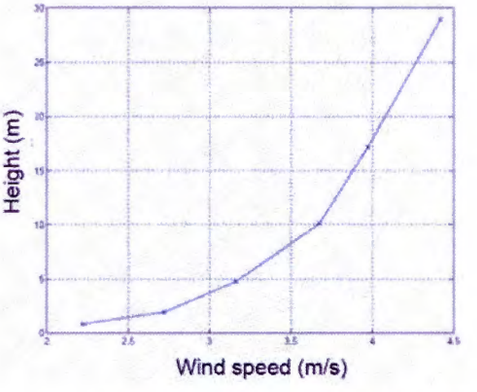

Figure 2: Wind speed and height

1.2 History of wind power

Since early recorded history, people have been harnessing the energy of the wind. Wind energy propelled boats along the Nile River as early as 5000 B.C. By 200 B.C., simple windmills in China were pumping water, while vertical-axis windmills (VAWT) with woven reed sails were grinding grain in Persia and the Middle East.

Figure 3: Old HAWT

Early in the twentieth century, windmills were commonly used across the Great Plains to pump water and to generate electricity (Figure 3).

New ways of using the energy of the wind eventually spread around the world. By the 11th century, people in the Middle East were using windmills extensively for food production; returning merchants and crusaders carried this idea back to Europe. The Dutch refined the windmill and adapted it for draining lakes and marshes in the Rhine River Delta. When settlers took this technology to the New World in the late 19th century, they began using windmills to pump water for farms and ranches, and later, to generate electricity for homes and industry.

Industrialization, first in Europe and later in America, led to a gradual decline in the use of windmills. The steam engine replaced European water-pumping windmills. In the 1930s, the Rural Electrification Administration's programs brought inexpensive electric power to most rural areas in the United States.

However, industrialization also sparked the development of larger windmills to generate electricity. Commonly called wind turbines, these machines appeared in Denmark as early as 1890. In the 1940s the largest wind turbine of the time began operating on a Vermont hilltop known as Grandpa's Knob. This

turbine, rated at 1.25 megawatts in winds of about 30 mph, fed electric power to the local utility network for several months during World War II.

The popularity of using the energy in the wind has always fluctuated with the price of fossil fuels. When fuel prices fell after World War II, interest in wind turbines waned. But when the price of oil skyrocketed in the 1970s, so did worldwide interest in wind turbine generators.

The wind turbine technology that followed the oil embargoes of the 1970s refined old ideas and introduced new ways of converting wind energy into useful power. Many of these approaches have been demonstrated in "wind farms" or wind power plants — groups of turbines that feed electricity into the utility grid — in the United States and Europe.

1.3 History of VAWT´s and HAWT´s

The first windmills were VAWT´s (Vertical Axis Wind Turbine). During the Middle Ages, horizontal axis windmills (HAWT) were built in Europe and used for mechanical tasks such as pumping water or grinding grain. These were the classical four-bladed old windmills that had a yawing system and were mounted on a big structure. These windmills lost popularity after the industrial revolution. At about the same time, water pumping windmills became popular in the United States, recognizable for their many blades and typically situated on a farm.

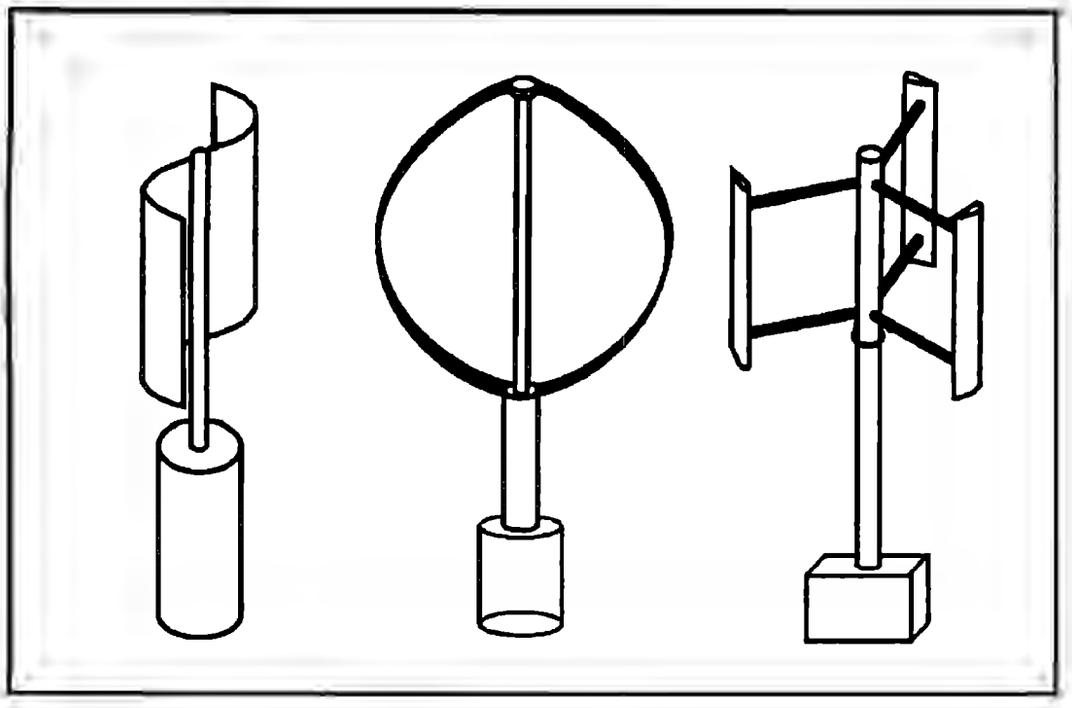

Figure 4: Types of VAWT
1. Savonius-Rotor 2. Darrius curved-bladed Rotor 3. Darrieus H-Rotor

One of the first attempts to generate electricity by using the wind was made in the United States by Charles Brush in 1888. Among the most important early turbines was the turbine developed by Marcellus Jacobs. Jacobs' turbine had three airfoil shaped blades, a battery storage and a wind wane keeping the turbine against the wind. During the 20th century the HAWTs continued to evolve, which resulted in bigger and more advanced turbines, leading to the modern HAWTs.

Vertical axis machines have been developed in parallel with HAWTs, but with less financial support and less interest. The finish engineer S.J. Savonius invented the Savonius turbine in 1922, see Fig. 4. In 1931, Georges Darrieus patented his idea to have a VAWT with straight or bent/curved blades, see Fig. 4. During the 1970s and 1980s vertical axis machines came back into focus when both Canada and the United States built several prototypes of Darrieus turbines. The prototypes proved to be quite efficient and reliable. According to a report from Sandia National Laboratories in the USA, the VAWTs felt victims to the poor wind energy market in the USA. The last of the Sandia VAWTs was dismantled in 1997 after cracks had been found on its foundation. In the 1980s the American company FloWind commercialised the Darrieus turbine and built several wind farms with Darrieus turbines. The machines worked efficiently but had problems with fatigue of the blades, which were designed to flex. The Eole, a 96m tall Darrieus turbine built in 1986, was the largest VAWT ever built with a rated maximum power of 3.8MW. It produced 12GWh of electric energy during the 5 years it was running and reached power levels of up to 2.7MW. The machine was shut down in 1993 due to failure of the bottom bearing.

The straight-bladed VAWT was also an invention included in the Darrieus patent. This turbine is usually referred to as the straight-bladed Darrieus turbine or the H-rotor, but has also been called giromill or cycloturbine (different concepts of the same invention) (see Fig. 4). In the United Kingdom, the H-rotor was investigated by a research team led by Peter Musgrove. The biggest H-rotor built in the UK was a 500kW machine, which was designed in 1989. In the 1990s, the German company Heidelberg Motor GmbH worked with development of H-rotors and they built several 300kW pototypes.

From this short historical review, it is clear that the first windmill was a VAWT but that later HAWTs received most attention. Could it be that it was only a coincidence that some researchers decided to develop the HAWT and that the VAWT only suffered from lack of interest? Now it is known that the HAWT is not

obviously better than the VAWT just because it long ago was randomly picked for large-scale development.

Another discipline where the choice between vertical and horizontal axis turbines is fundamental is tidal current power conversion. For tidal current power vertical axis turbines are in favour in research projects conducted in several countries.

1.4 Comparative study between VAWT and HAWT

A comparative study of the two wind turbines is presented from the most important aspects including structural dynamics, control system, maintenance, manufacturing and electrical equipment. The straight-bladed (or H-Rotor) and curved-bladed Darrieus turbine is referred to together as VAWT´s because of similar characteristics, however the view is concentrated on the H-Rotor.

The main difference between VAWTs and HAWTs (see fig. 5) is the VAWT's ability to accept wind from any direction, i.e. it is omni-directional. This has several advantages. The turbine does not require a yaw system, which is costly and could fail during operation. Furthermore, with an omni-directional turbine there are no power losses during the time it takes for the turbine to yaw or during short wind gusts with temporary changes in wind direction. An omni-directional turbine can be situated at places where the wind is turbulent and where the wind direction changes often. Investigations indicate a clear advantage in using VAWTs at rooftops. Furthermore, the VAWT is less noisy than the HAWT, which becomes even more important in urban areas.

Figure 5: Modern HAWT

The vertical rotational axis of a VAWT allows the generator to be located at the bottom of the tower. This makes installation, operation and maintenance much easier.

Direct drive here denotes a solution where the turbine is directly, through a shaft, connected to the rotor of the generator. By using a direct drive generator, the gearbox is excluded from the system. A gearbox is often associated with breakdown and need of maintenance.

The blades of a HAWT have to be self-supporting since they are only attached at the root. The blades of an H-rotor, which are much easier to manufacture, are supported by support arms, which usually are attached to the centre of the blades. However, the support arms add extra structure and mass to the turbine.

HAWTs have relatively constant torque. VAWTs have an inherent torque ripple. The torque ripple is caused by the continuously changing angle of attack between the blades and the apparent wind.

The performance of a wind turbine depends on the power coefficient, C_P, which states how much of the energy in the wind that is absorbed by the wind turbine. For a HAWT, the C_P (limited by the betz criteria) value is usually between 0.40 and 0.50. It is difficult to state the exact value of C_P for VAWTs since there are few turbines operating. Values of C_P are therefore based on theoretical studies and on experimental results from different studies and are usually around 0.40. Power curves for the three different turbines can be seen in Fig. 6. The power coefficient, C_P, is shown as a function of the tip speed ratio. Fig. 6 indicates that the three turbines operate at different optimum tip speed ratios, which affects the noise level. The VAWTs have almost as good efficiency as the HAWT.

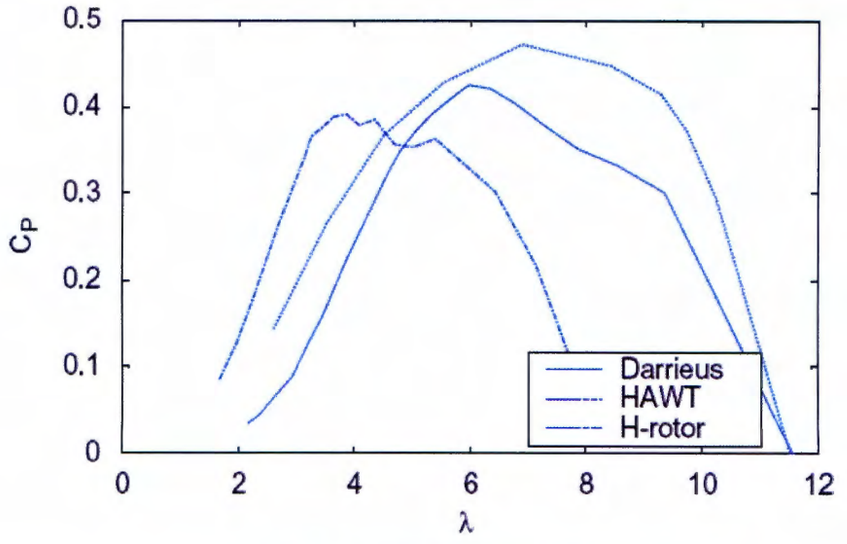

Figure 6: Power curve of different turbines

HAWTs are self-starting at a low wind speed. VAWTs have poor starting torque due to the blade stall condition at high angles of wind attack. The H-rotor has better selfstarting ability than the Darrieus turbine.

The H-rotor is expected to produce much less noise than a HAWT. There are two main sources for wind turbine noise; aerodynamic noise from the turbine's blade tips and mechanical noise from the drive train components.

Significant differences between wind turbines depending on the direction of their axis of rotation have been presented. This comparative study has shown that VAWT´s are advantageous to HAWT´s in several aspects. When comparing the two types of VAWT´s considered here, the H-rotor seems more advantageous than the Darrieus turbine. The strength of the H-rotor concept is the possibility to keep the structure simple. The H-rotor does not require any yaw mechanism, pitch regulation or gearbox and therefore has few movable parts. Another advantage is its expected low need of maintenance.

The HAWT is already established on the global market and it still has to be proven that VAWT´s are an interesting alternative for wind power generation and more funding and interested researchers are needed to do so.

1.5 Current situation of wind power

The need for development of renewable energy has been increasing because of the continuing oil crisis and environmental pollution, and one of these resources is wind energy. Wind-power is the world's fastest-growing energy source, with installations increasing by about 30% a year. It is renewable, it does not pollute while in operation, it entails no future liabilities associated with the decommission of obsolete plants, it lends itself to dual land use with agriculture, natural habitats, or human residence, and, perhaps most important, it is ideally suitable to produce hydrogen as a substitute fuel.

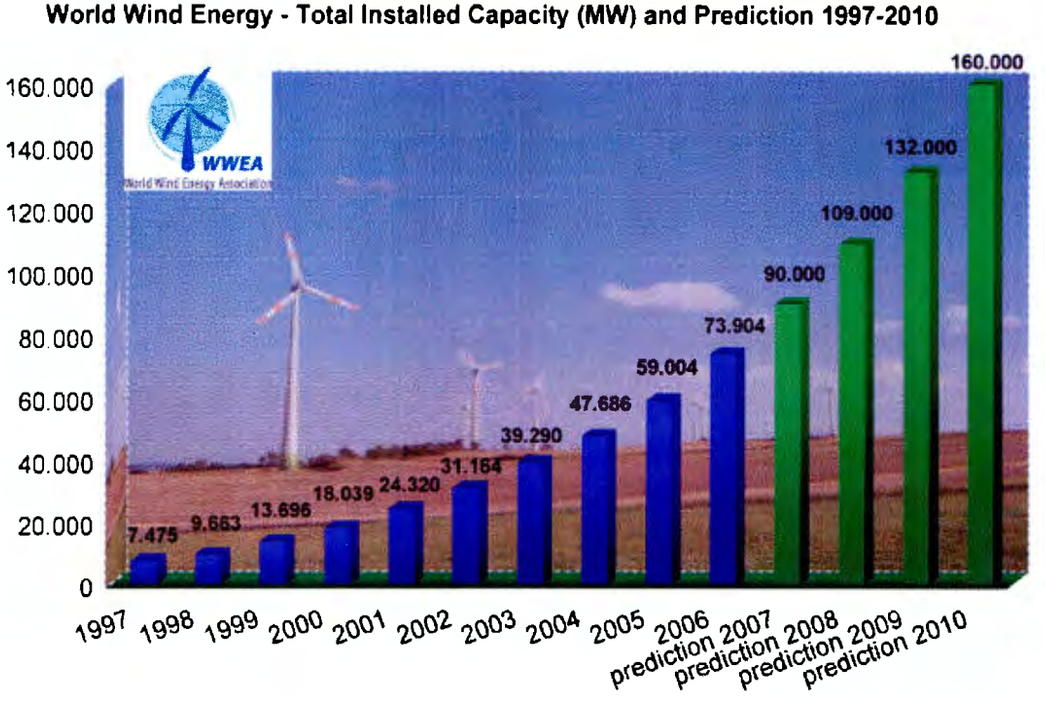

Figure 7: Wind power capacity worldwide 1997-2010

The survey on demand in USA and Europe showed that about 12% of the global power generation will be substituted with wind power by 2020. In Denmark, wind power covers almost 20% of their power consumption. In China, wind energy occupies only 0.1% now, but they are developing commercial wind power system by cooperation with advanced countries such as Spain. They are

also developing small scale home use wind power system for the people in the western regions that have insufficient in electricity. But still Wind power is in comparison to other energy resources expandable, shown in the following figure 8.

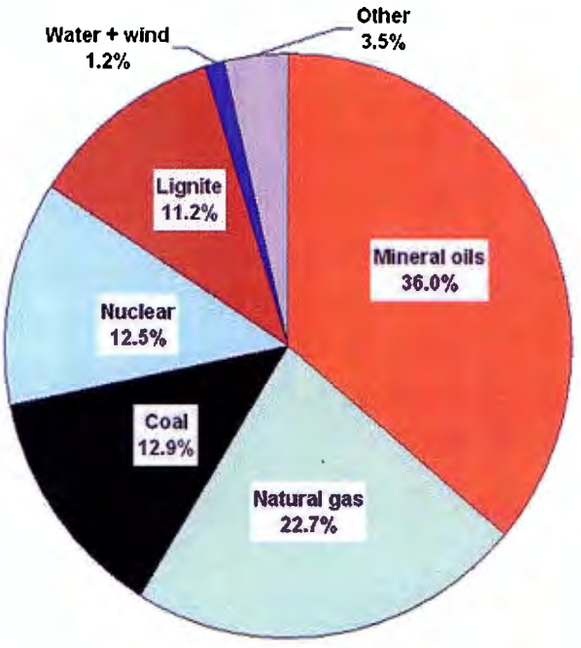

Figure 8: Primary energy distribution, 2007

It is a fact that due to economics-of-scale reasons cost effectiveness of wind-turbines increases with size. During the last 25 years the size of the state-of-the-art wind machine has been increasing systematically but the actual technology of horizontal-axis wind turbines would ultimately reach its limits. Very large sizes would create a number of significant problems in rotor design, and the low rotational speed associated with large radius would complicate the coupling with the electrical generator. Hence, it is worthwhile to explore innovative concepts to overcome the size limits of the actual wind-power technology and also has been able to exploit the renewable energy potential that high-windspeed regions offer. To this end, an innovative concept of small scale wind turbine, like the Darrieus H- rotor, has been introduced.

2.0 Theoretical background

2.1 Betz criteria

The efficiency of a wind turbine is measured as the ratio between the energy extracted from the wind to perform useful work and the total kinetic energy of the wind without the presence of a wind turbine. To understand the reasoning behind Betz' Law, consider a 100% efficiency, i.e., extracting all the kinetic energy from the wind and thus bringing the air to a standstill. The paradox of bringing the air to a stop means that there's no way for the air to drive a rotating machine, so no useful work can be extracted. Now consider the other extreme, i.e., the wind turbine doesn't reduce the wind speed at all. Again conservation of energy dictates that no useful work will be accomplished by the wind turbine. Clearly the maximum theoretical efficiency lies somewhere between these two extremes. Betz' Law simply and elegantly proves that the maximum efficiency of a wind turbine can't exceed 59%.

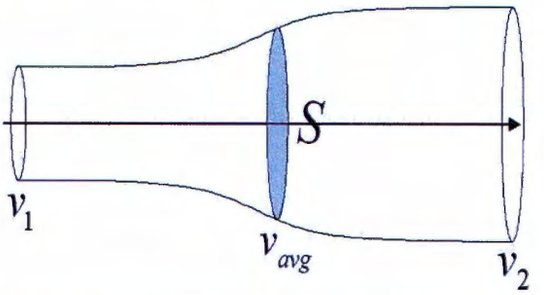

Figure 9: Schematic of fluid flow through an actuator

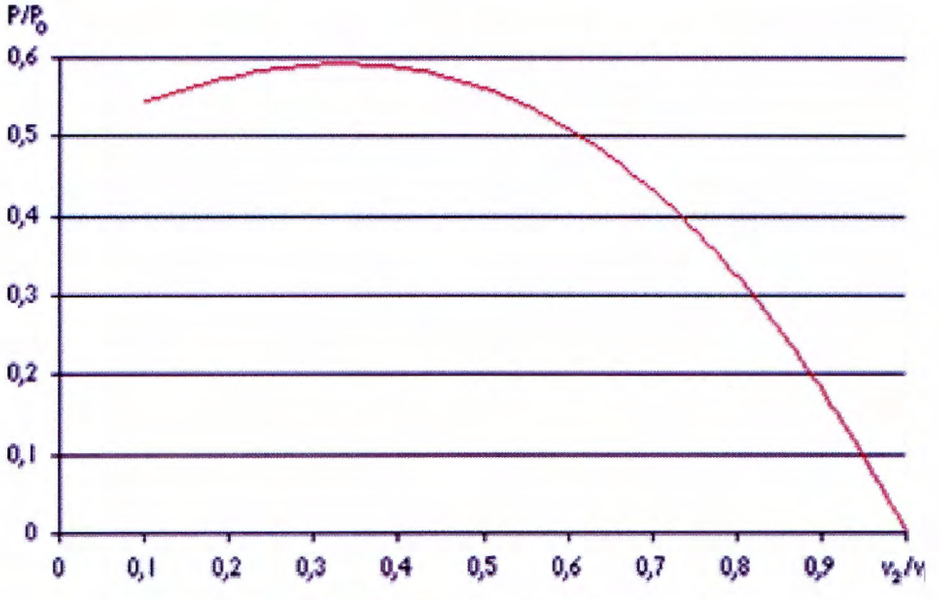

Figure 10: The Betz criteria, P/P_0 as a function of v_2/v_1

2.2 TIP speed ratio

The tip Speedy ratio λ (lambda) or TSR for wind turbines is the ratio between the rotational speed of the tip of a blade and the actual velocity of the wind. If the velocity of the tip is exactly the same as the wind speed the tip speed ratio is 1. A tip speed ratio above 1 indicates some amount of lift, below 1 usually indicates drag. A high tip speed ratio indicates mostly a better efficiency but is usually also related to a higher noise level and a heavier design.

$$\lambda = \frac{V_t}{V_w} \tag{1}$$

It has been shown empirically that the optimum tip speed ratio for maximum power output occurs at:

$$\lambda_{\max power} = \frac{4\pi}{N} \tag{2}$$

where N is the number of blades.

Because the H-Rotor has 3 blades it means that the optimal TSR is by 4.189.

2.3 Lift and drag definition

A total aerodynamic force is generated when a stream of air flows over and under an airfoil that is moving through the air. The point at which the air separates to flow about the airfoil is called the point of impact.

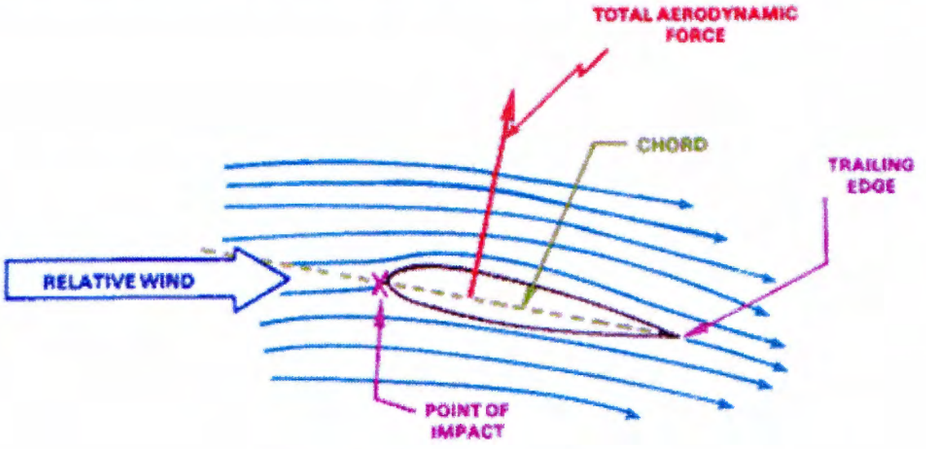

Figure 11: Airflow around an airfoil

A high pressure area or stagnation point is formed at the point of impact. Normally the high pressure area is located at the lower portion of the leading edge, depending on angle of attack. This high pressure area contributes to the overall force produced by the blade.

The figure 11 also shows airflow lines that illustrate how the air moves about the airfoil section. Notice that the air is deflected downward as it passes under the airfoil and leaves the trailing edge. Remember Newton's third law which states "every action has an equal and opposite reaction." Since the air is being deflected downward, an equal and opposite force must be acting upward on the airfoil. This force adds to the total aerodynamic force developed by the airfoil. At very low or zero angles of attack, the deflection force or impact pressure may exert a zero positive force, or even a downward or negative force.

Air passing over the top of the airfoil produces aerodynamic force in another way. The shape of the airfoil causes a low pressure area above the

airfoil according to Bernoulli's Principle, and the decrease in pressure on top of the airfoil exerts an upward aerodynamic force. Pressure differential between the upper and lower surface of the airfoil is quite small - in the vicinity of 1 percent. Even a small pressure differential produces substantial force when applied to the large area of a rotor blade.

The total aerodynamic force, sometimes called the resultant force, may be divided into two components called lift and drag. Lift acts on the airfoil in a direction perpendicular to the relative wind. Drag is the resistance or force that opposes the motion of the airfoil through the air. It acts on the airfoil in a direction parallel to the relative wind.

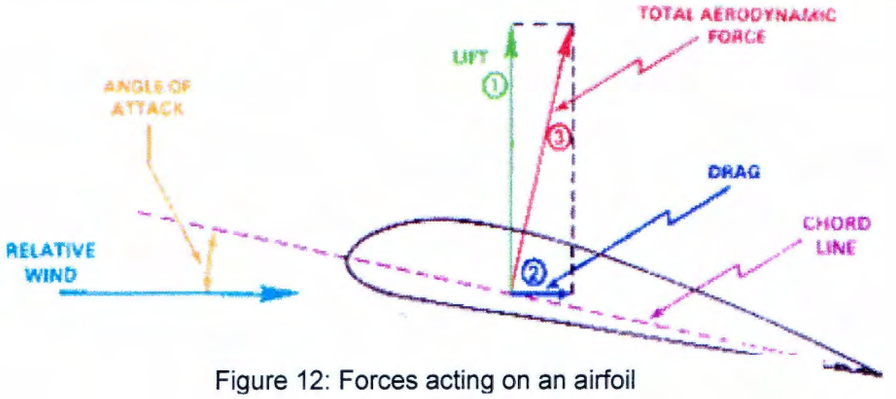

Figure 12: Forces acting on an airfoil

Many factors contribute to the total lift produced by an airfoil. Increased speed causes increased lift because a larger pressure differential is produced between the upper and lower surfaces. Lift does not increase in direct proportion to speed, but varies as the square of the speed. Angle of attack also has an effect on the lift produced. Lift increases as the angle of attack increases up to the stalling angle of attack. Stall angle varies with different blades and is the point at which airflow no longer follows the camber of the blade smoothly. Air density is another factor that directly influences lift.

Lift and drag force:

$$L = \frac{1}{2} \cdot C_l \cdot \rho \cdot A \cdot V_W \quad (3)$$

$$D = \frac{1}{2} \cdot C_d \cdot \rho \cdot A \cdot V_W \quad (4)$$

Two design factors, Airfoil Shape and Airfoil Area are primary elements that determine how much lift and drag a blade will produce. Any change in these design factors will affect the forces produced.

Normally an increase in lift will also produce an increase in drag. Therefore, the airfoil is designed to produce the most lift and the least drag within normal speed ranges.

2.4 Airfoil shape and lift/drag coefficient

As aforementioned the lift/drag coefficient C_d/C_l and therefore the lift/drag force depends on the angle of attack α and the Airfoil design. The various types of Airfoils are centralized in the NACA series. The NACA airfoils are airfoil shapes for aircraft wings developed by the National Advisory Committee for Aeronautics (NACA). The shape of the NACA airfoils is described using a series of digits following the word "NACA". Experiences have shown that the NACA 6 series has the most advantageous shapes for an H-Rotor, because they are designed to increase the amount of laminar flow and reduce drag. With the help of the special software DesignFOIL you can simulate the chosen airfoil type in a virtual wind channel and get for the calculation important dates of C_d and C_l.

Firstly the shape of airfoil can be selected in the manageable program surface. An airfoil of the type NACA 63-018 is chosen. This airfoil profile was found to have the most optimal performance for Darrieus wind turbines.

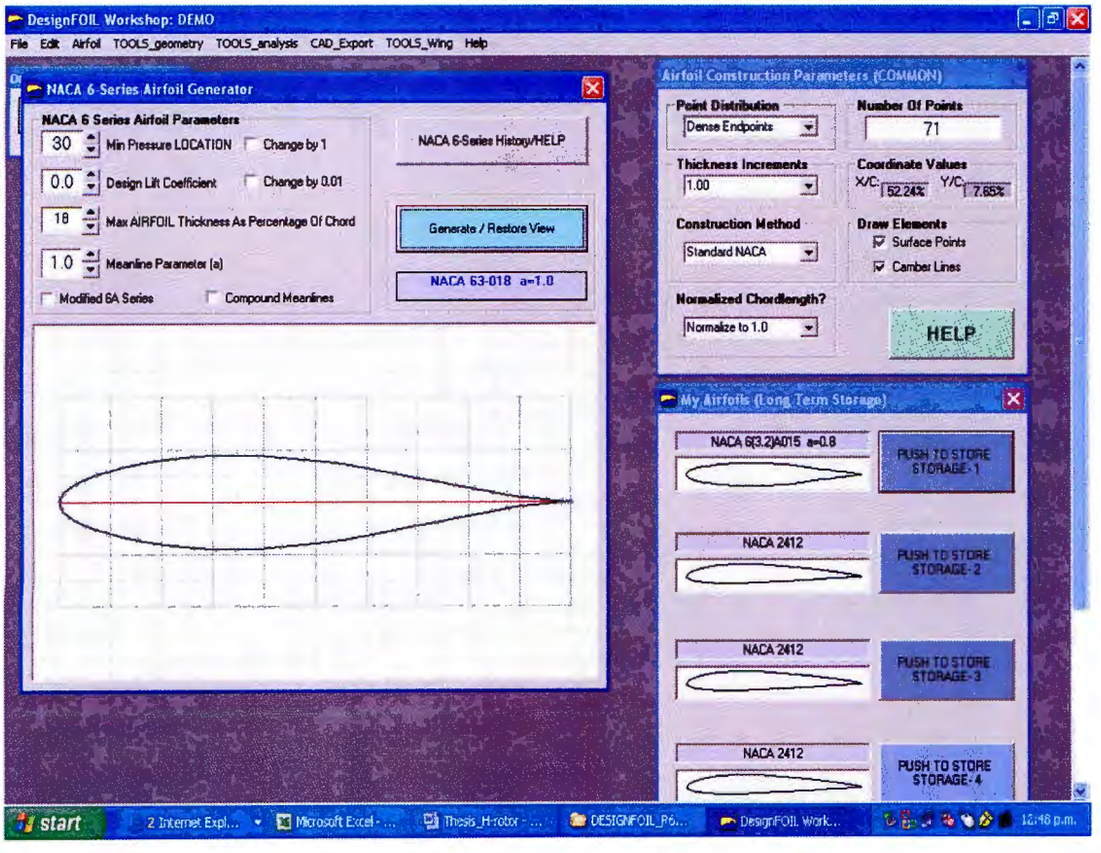

Figure 13: Airfoil simulation program DesignFOIL

After saving the favored airfoil shape with "Generate/Restore View" we can diversify the environment variables with the path "TOOLS_analysis < Atmosphere Simulator", like altitude, reynold number (in our case 250 000) or wind speed V_w = 6 m/s (according Fig. 1 a very common wind speed). Also the wind tunnel option can be altered (TOOLS_analysis < Virtual wind tunnel options).

The simulation can now be started with the results shown in the following window (Figure 14).

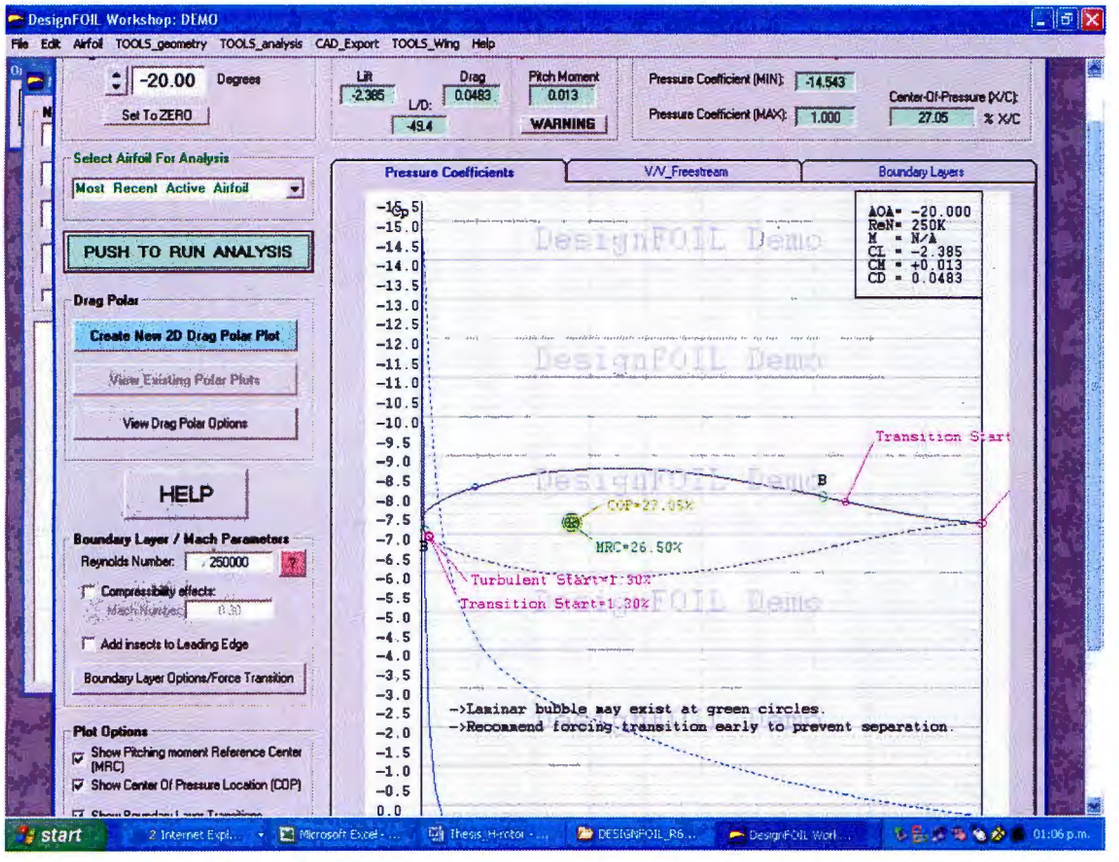

Figure 14: Virtual wind tunnel results

Therefore the calculation important Coordinates of C_d and C_l (seen in Appendix I) can be seen by pressing the button "Create New 2D Drag Polar Plot". The shown plot can be transferred into Excel, so it can be easily used for the next steps of the calculation (Fig. 15 and 16).

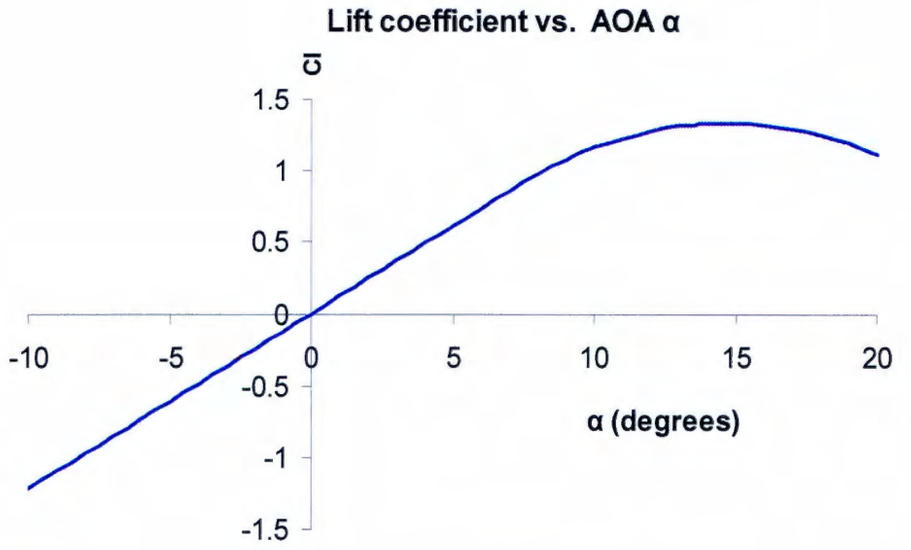

Figure 15: C_l vs. angle of attack

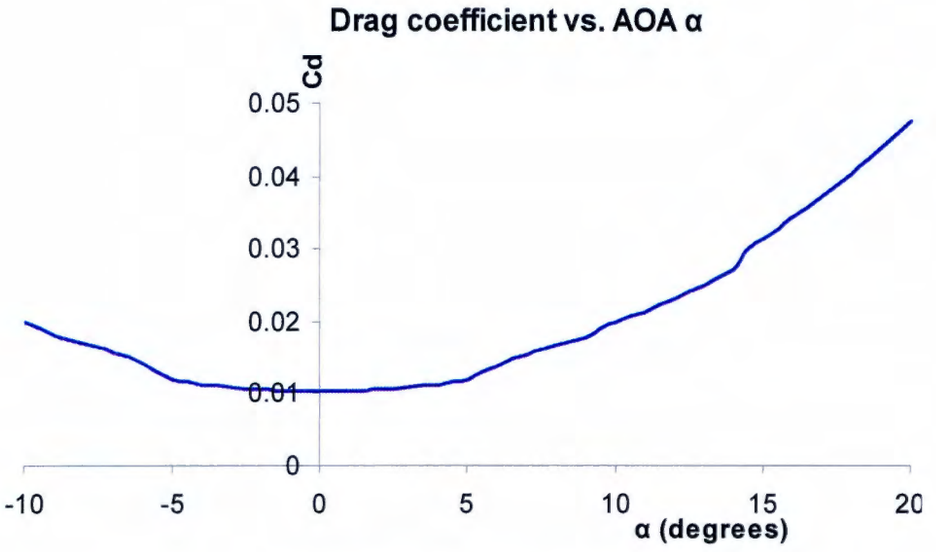

Figure 16: C_d vs. angle of attack

At higher angles of attack, it is apparent that drag increases significantly and lift drops off. High angles of attack also caused separation further up along the airfoil, increasing drag. At very high AOA, this drag takes over. Especially the diagram of C_l shows that the value reaches the maximum between AOA α of 10° and 20°. In this ambit the turbine works most efficiently.

3.0 Calculation

3.1 General mathematical expression for aerodynamic analysis

Though the straight-bladed Darrieus-type VAWT is the simplest type of wind turbine, its aerodynamic analysis is quite complex. Before comparative analysis of the main aerodynamic models, the general mathematical expressions, which are common to most of the aerodynamic models, are described in this section.

3.1.1 *Power available from the wind*

The Power available in the wind is proportional to the cube of the wind speed and the area of the turbine A:

$$A = 2 \cdot R \cdot l \tag{5}$$

where R and l are the radius and length of the blade, respectively. The total power available is given as

$$P_a = \frac{1}{2} \cdot \rho \cdot A \cdot V_w^{\,3} \tag{6}$$

where ρ is the density of the air and Vw is the undisturbed wind speed. But like already known is the available power limited of the Bertz criteria (see 2.1). It is obvious that the power depends heavily on the wind speed.

3.1.2 *Variation of local angle of attack*

The flow velocities in the upstream and downstream sides of the Darrieus-type VAWTs are not constant as seen in Fig. 17. From this figure one can

observe that the flow is considered to occur in the axial direction. The chordal velocity component V_c and the normal velocity component V_n are, respectively, obtained from the following expressions:

$$V_c = R\omega + V_a \cos\theta \tag{7}$$

$$V_n = V_a \sin\theta \tag{8}$$

where V_a is the axial flow velocity (i.e. induced velocity) through the rotor, ω is the rotational velocity, R is the radius of the turbine, and θ is the azimuth angle. Referring to Fig. 17, the angle of attack (α) can be expressed as

$$\alpha = \tan^{-1}\left(\frac{V_n}{V_c}\right) \tag{9}$$

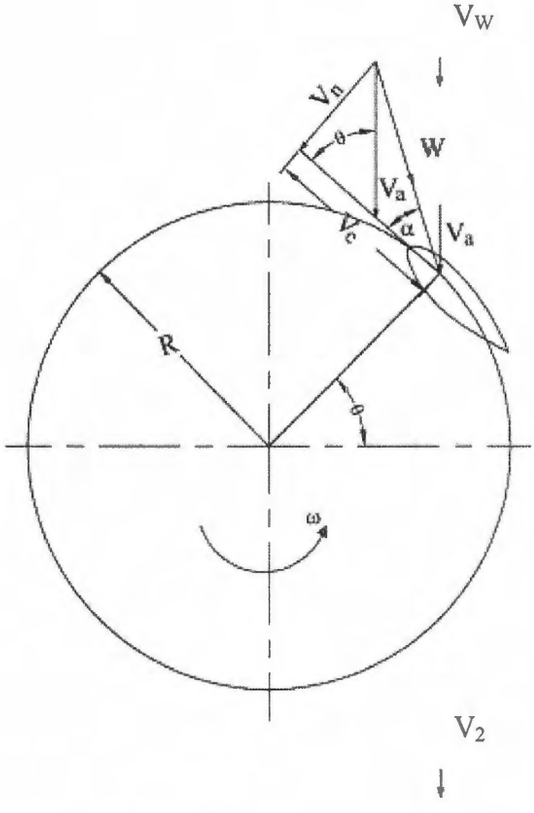

Figure 17: Flow velocities of straight-bladed Darrieus-type VAWT

Substituting the values of V_n and V_c and non-dimensionalizing,

$$\alpha = \tan^{-1}\left[\frac{\sin\theta}{(R\omega/V_W)/(V_a/V_W)+\cos\theta}\right], \qquad (10)$$

where V_W is the freestream wind velocity. If we consider blade pitching then,

$$\alpha = \tan^{-1}\left[\frac{\sin\theta}{(R\omega/V_W)/(V_a/V_W)+\cos\theta}\right]-\gamma, \qquad (11)$$

where γ is the blade pitch angle.

3.1.3 *Variation of local relative flow velocity*

The relative flow velocity (W) can be obtained as (Fig. 18),

$$W = \sqrt{V_c^2 + V_n^2} \qquad (12)$$

Inserting the values of V_c and V_n (eqs. (7) and (8)) in eq. (13), and non-dimensionalizing, one can find velocity ratio as,

$$\frac{W}{V_W} = \frac{W}{V_a}\cdot\frac{V_a}{V_W} = \frac{V_a}{V_W}\cdot\sqrt{\left[\left(\frac{R\omega}{V_W}/\frac{V_{au}}{V_W}\right)+\cos\theta\right]+\sin^2\theta}, \qquad (13)$$

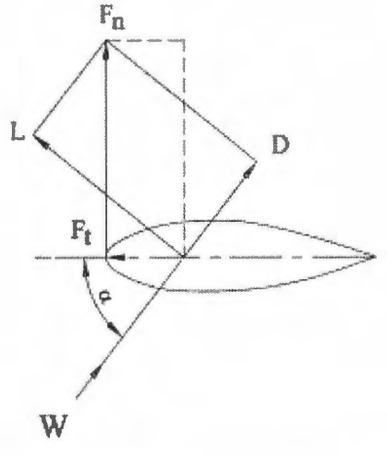

Figure 18: Force diagram of a blade airfoil

3.1.4 *Variation of tangential and normal forces*

The directions of the lift and drag forces and their normal and tangential components are shown in Fig. 18. The tangential force coefficient (C_t) is basically the difference between the tangential components of lift and drag forces. Similarly, the normal force coefficient (C_n) is the difference between the normal components of lift and drag forces. The expressions of C_t and C_n can be written as

$$C_t = C_l \sin\alpha - C_d \cos\alpha \tag{14}$$

$$C_n = C_l \cos\alpha + C_d \sin\alpha \tag{15}$$

The net tangential and normal forces can be defined as

$$F_t = C_t \frac{1}{2} \rho \cdot f \cdot l \cdot W^2 \tag{16}$$

$$F_n = C_n \frac{1}{2} \rho \cdot f \cdot l \cdot W^2 \tag{17}$$

Where ρ is the air density, f is the blade chord and l is the length of the blades.

3.1.5 *Calculation of total torque*

Since the tangential and normal forces represented by Eqs. (16) and (17) are for any azimuthal position, they are considered as a function of azimuth angle θ. Average tangential force (F_{ta}) on one blade can be expressed as

$$F_{ta} = \frac{1}{2\pi} \int_0^{2\pi} F_t(\theta) d\theta \tag{18}$$

The total torque (Q) for the number of blades (N) is obtained as

$$Q = N F_{ta} R \tag{19}$$

3.1.6 *Power output*

The total power (P) can be obtained as

$$P = Q \cdot \omega \tag{20}$$

3.2 Definition of V_a

In the past, several mathematical models, based on several theories, were prescribed for the performance prediction and design of Darrieus-type VAWT´s by different researchers. Some key components of the calculation are already known, like C_l and C_d investigated with DesignFOIL. To get the induced axial velocity V_a some computational models are taken in to account. According to literature survey, the most studied and best validated models can be broadly classified into three categories – Momentum model, Vortex model and Cascade model.

3.2.1 *Momentum model*

Different momentum models (also specified as Blade Element/Momentum or BEM model) are basically based on calculation of flow velocity through turbine by equating the streamwise aerodynamic force on the blades with the rate of change of momentum of air, which is equal to the overall change in velocity times the mass flow rate. The force is also equal to the average pressure difference across the rotor. Bernoulli´s equation is applied in each streamtube. The main drawback of these models is that they become invalid for large tip speed ratios and also for high rotor solidities because the momentum equations in these particular cases are inadequate.

3.2.2 *Single streamtube model*

In 1974 Templin proposed the single streamtube model which is the first and most simple prediction method for the calculation of the performance characteristics of a Darrieus-type VAWT´s. In this model the entire turbine is assumed to be enclosed within a single streamtube as shown in Fig. 19. This model first incorporated the concept of the windmill actuator disc theory into the analytical prediction model of a Darrieus-type VAWT. In this theory the induced velocity V_a is assumed to be constant throughout the disc.

In the assumption, the actuator disc (see Fig. 9) is considered as the surface of the imaginary body of revolution. It is assumed that the flow velocity is constant throughout the upstream and downstream side of the swept volume.

Now, according to Gluert Actuator Disk theory, the expression of the uniform velocity through the rotor is

$$V_a = \frac{V_w + V_2}{2} \quad , \tag{21}$$

where V_2 is the wake velocity. All the calculations in this model are performed for a single blade whose chord equals the sum of the chords of the actual rotor´s blades.

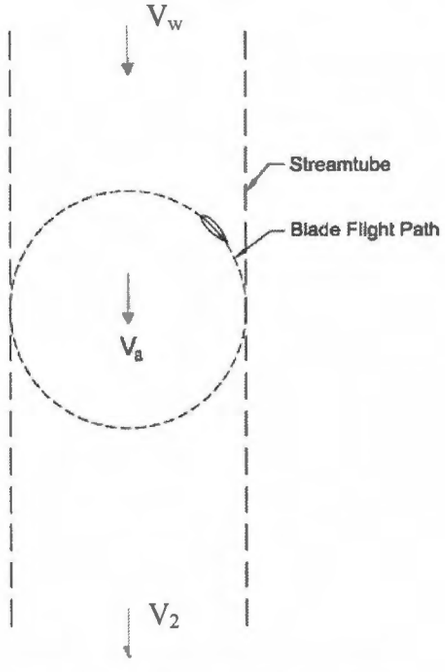

Figure 19: Schematic of single streamtube model

3.2.3 *Determination of V_a*

To solve the equation (21) we need to know the variable V_2, which depends on many factors. To investigate the wake velocity V_2 it is necessary to make a simplification considering the betz criteria in chapter 2.1.

The betz law says that the maximum power that can be reached is 59% of the available wind power (eq. (6)), but experiences had shown that for a good performing Darrieus wind turbine the average power coefficient Cp is around 40% (with λ=4; seen in Fig. 6). In the case of the turbine in this thesis the estimated range of P/P_0 ($=C_p$) is between 30% and 40%, because of inaccuracies in the design process a.s.o. According Fig. 20 the range of the ratio v_2/v_1 is between 0,73 and 0,81. For the calculation the arithmetic mean 0,77 is chosen.

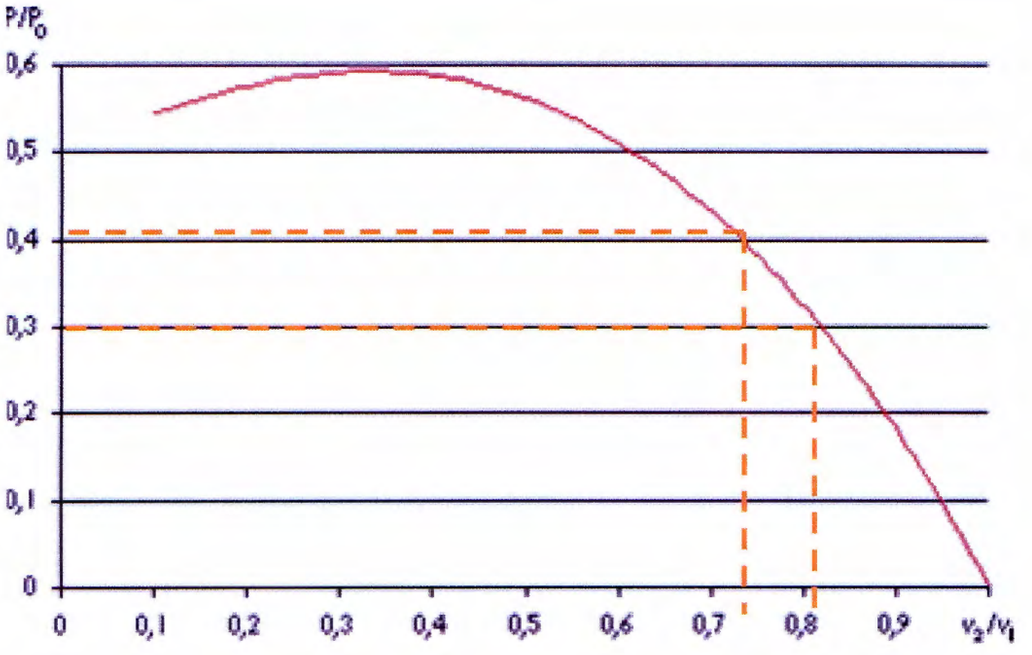

Figure 20: Investigation of V_a with the betz criteria

In the following calculation we get the wake velocity V_2:

$$V_1 = V_w$$

$$V_2 = 0{,}77 \cdot V_w = 0{,}77 \cdot 6\frac{m}{s}$$

$$V_2 = 4{,}62\frac{m}{s}$$

Then the axial flow velocity V_a (equ. (21)) is:

$$V_a = \frac{V_w + V_2}{2} = \frac{6 + 4{,}62}{2}\frac{m}{s}$$

$$V_a = 5{,}31\frac{m}{s}$$

Thus we say that induced velocity V_a is at all times constant, what simplifies the calculation.

3.3 Relation between α and θ

The 3-D turbine can be modeled as a 2-D cross section, as shown below (Fig. 21).

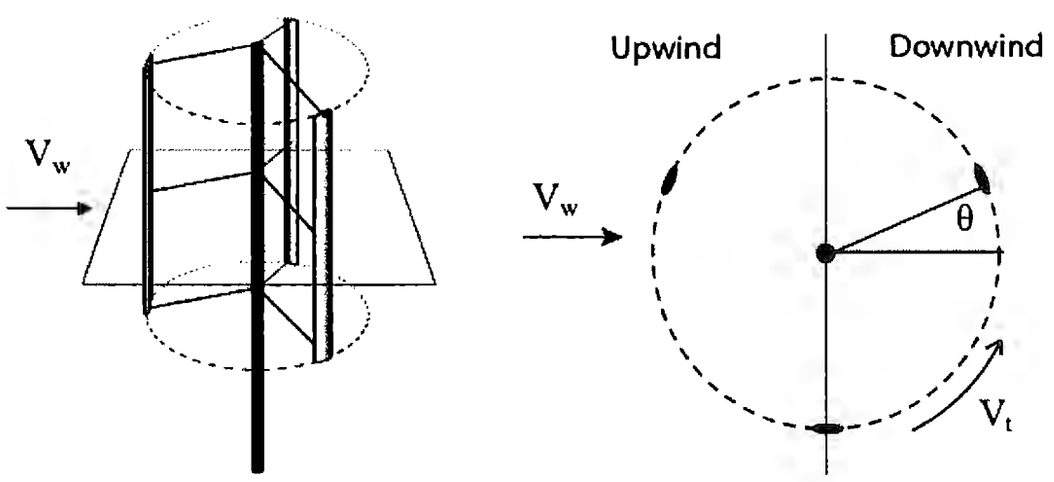

Figure 21: H-Rotor model

A positive angle of attack is when the nose of the airfoil points upwards with respect to the oncoming wind. To calculate torque, angle of attack α was determined for each point in the cycle. After putting eqs. (7) and (8) in (9) the equation for angle of attack is given as:

$$\alpha = \arctan\left(\frac{V_a \sin\theta}{R\omega + V_a \cos\theta}\right) \tag{22}$$

where V_a is the axial flow velocity, V_t (= Rω) is the tangential speed of the airfoil and θ gives the position of the airfoil in the rotational cycle. The TIP speed ratio λ (TSR) is seen in eq. (1). Then it is inserted equation (1) in equation (22) to see the interrelation between angle of attack α and the azimuth angle θ against the tip speed ratio λ.

$$\lambda = \frac{V_t}{V_W} = \frac{R\omega}{V_w} \Rightarrow R\omega = \lambda \cdot V_W$$

$$\alpha = \arctan\left(\frac{V_a \sin\theta}{V_w \lambda + V_a \cos\theta}\right) \tag{23}$$

At low TIP speed ratio the angles of attack get very hight, as shown in the plots Fig. 22 and 23.

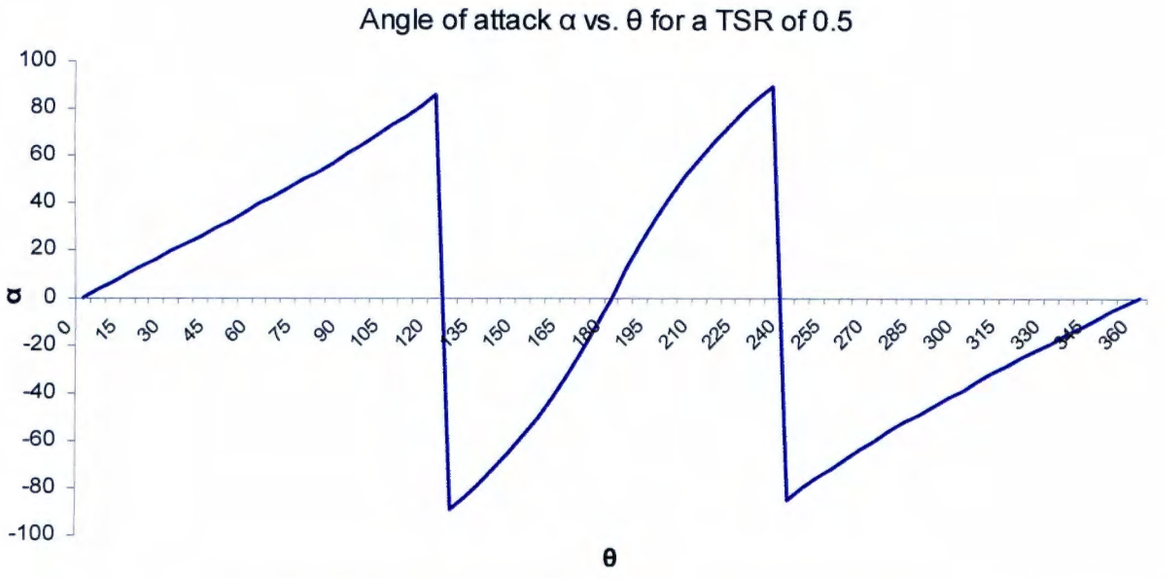

Figure 22: Angle of attack α vs. θ, TSR= 0.5 (Microsoft Excel)

TSR of 0.5 means that the wind speed V_w is higher than the tangential speed V_t of the blade, what increases drag and for this the H-Rotor has bad self-starting properties. Also notable is that by a TSR of 1, which means $V_t = V_w$, (see Fig. 23) the run has only one maxima/minima and is more homogenous than with TSR of 0.5 (Fig. 22).

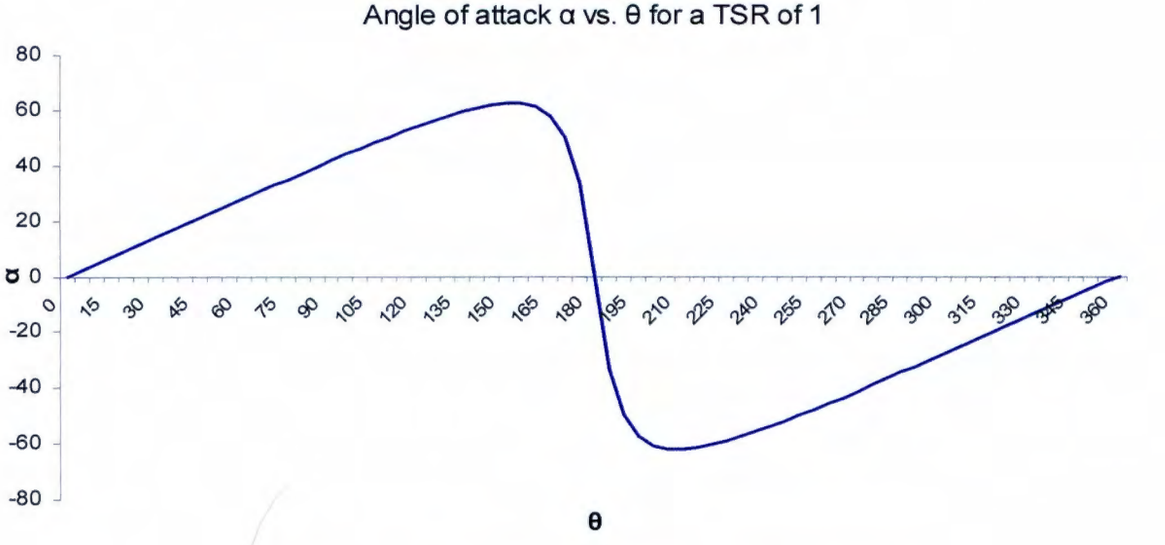

Figure 23: Angle of attack α vs. θ, TSR= 1 (Microsoft Excel)

Angles of attack for higher TSR are much smaller. The next plot shows angles of attack for higher TIP speed ratios (Fig. 24).

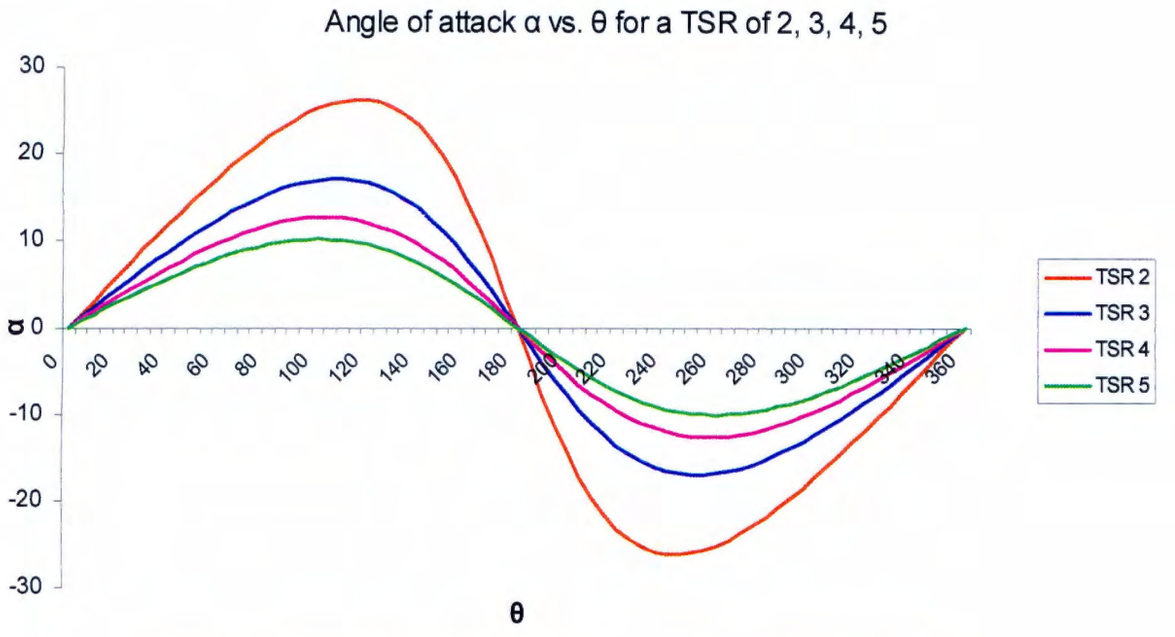

Figure 24: Angle of attack α vs. θ, TSR of 2, 3, 4 and 5 (Microsoft Excel)

Now considering in the Figures 15 and 16:

The value of C_l is decreasing when α is above 20° that means that the lift force L (seen in eq. (3)), which is responsible for the torque, is also decreasing. In Figure 16 is shown that α increases in both the positive and negative fields, affected the C_d which also increases, what lead to a higher drag force D (eq. (4)). Hence according to Fig. 15 the best performance can be reached when α is between 10° and 20°. Looking at Figure 24 the runs of TSR 2, 3 and 4 achieve this condition.

3.4 Solution of the calculation

3.4.1 *Investigation of the equations of C_l and C_d with EES*

The hole to power P solved equation is seen in Appendix ||. However the problem is, that the equation includes 5 variables, namely C_d, C_l, α, θ and P. Which means that, at first glance it is mathematically impossible to solve the equation. Hence the aim is to eliminate 3 parameters.
It is known that C_d and C_l depends on the Angle of Attack α (see 2.4) and with the help of the airfoil software DesignFOIL we get the coordinates of C_d, C_l versus α (see Appendix I).

The next step is to get a mathematical interrelation which shows the connection between these 3 variables. The software EES, however, can help to find the solution. This program can create a mathematical equation by means of coordinates.

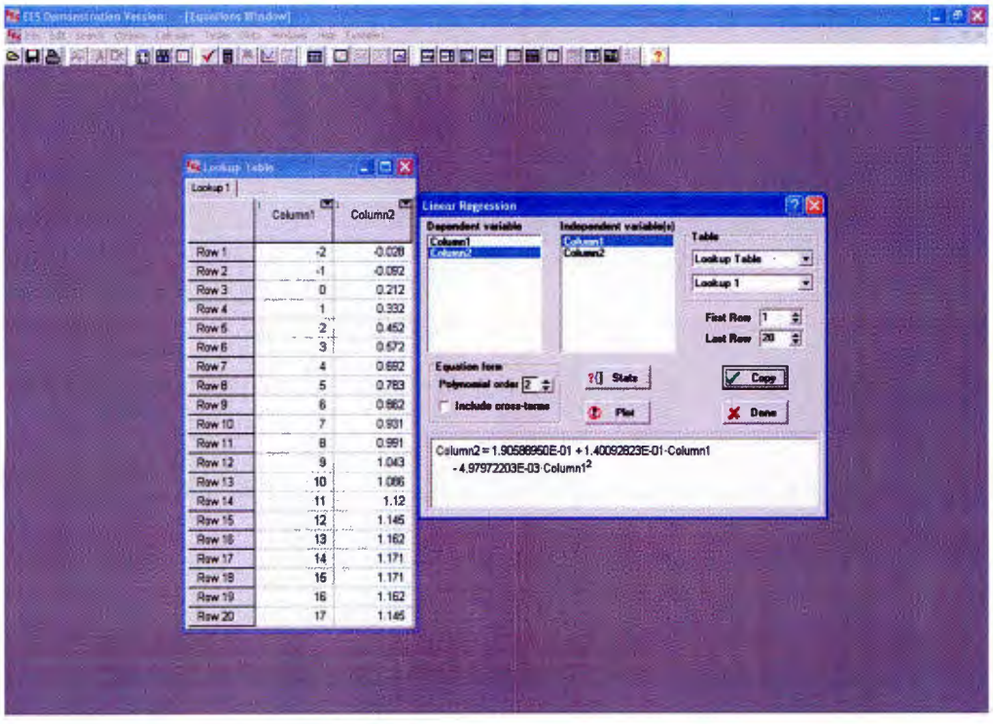

Figure 25: Software EES

After putting the coordinates of AOA α, C_d and C_l (see Appendix I) in a "New Lookup Table" first you click the "solve" button to get the plot. Afterwards the function "Linear Regression" in the menu "Table" finds a mathematical equation of the two variables. The program additionally gives the option to select the polynomial order. After clicking "Fit" the equation is shown and with the Mircosoft Excel program a graph can be made. The following plots (Fig. 26 and 27) point the approximation of the software ESS on the original dates of DesignFOIL.

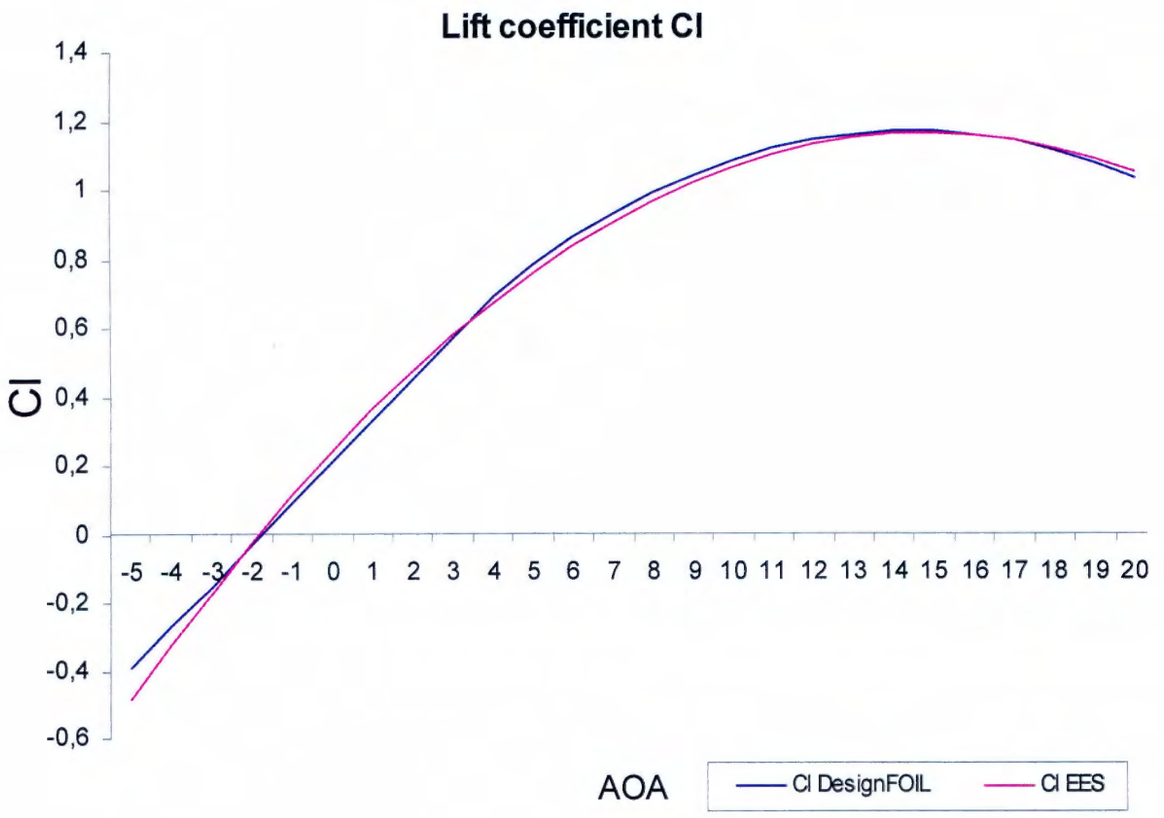

Figure 26: Comparison of lift coefficient C_l

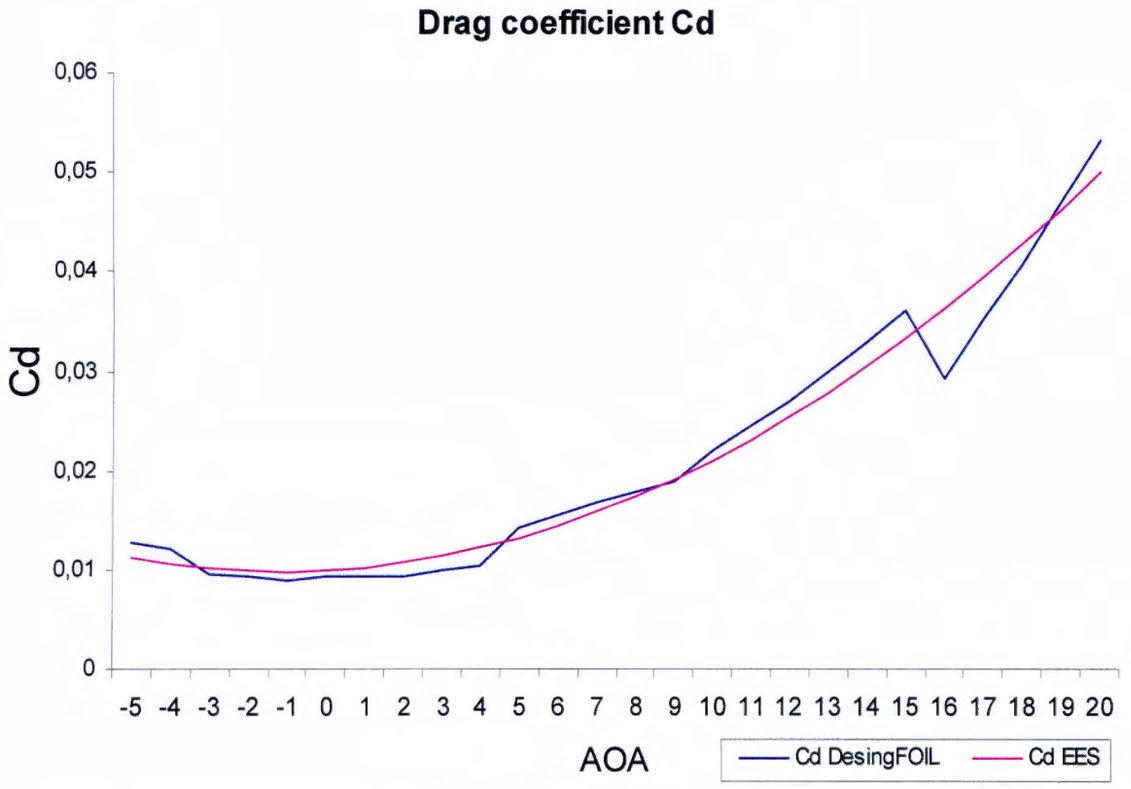

Figure 27: Comparison of drag coefficient C_d

The two investigated equations of $C_l(\alpha)$ and $C_d(\alpha)$ are:

$$C_l = 0{,}243461538 + (0{,}124433516 \cdot \alpha) - (4{,}18992674 \cdot 10^3 \cdot \alpha^2) \quad (24)$$

$$C_d = 9{,}95538462 \cdot 10^3 + (2{,}10967033 \cdot 10^4 \cdot \alpha) + (8{,}95115995 \cdot 10^5 \cdot \alpha^2) \quad (25)$$

Now with the equation (23) the parameter α is eliminated, however in eqs. (24) and (25) the value of α is in degrees. Now the overall calculation is almost solved, because the entire equation (seen in appendix II) includes only two parameters (P, θ) that it can be illustrated $P_{(\theta)}$.

3.4.2 *Determination of the values R, l, S and f*

Now the coordinates of DesignFOIL are calculated with the wind speed V_w = 6m/s (see 2.4). All the other variables (TSR λ, radius R, blade length l and chord length f) can be modified. For this construction the following values of the variables are chosen: TIP speed ration λ = 4 (see equation (2)), Radius R = 0,4 m, length of the blade l = 0,8 m and number of blades N = 3.
The chord length of the blade depends on the solidity:

$$S = \frac{N \cdot f}{2 \cdot R} \tag{26}$$

The H-Rotor will operate during a TIP speed rate between 1 and 5. The following plot shows the dependence between solidity and the TSR.

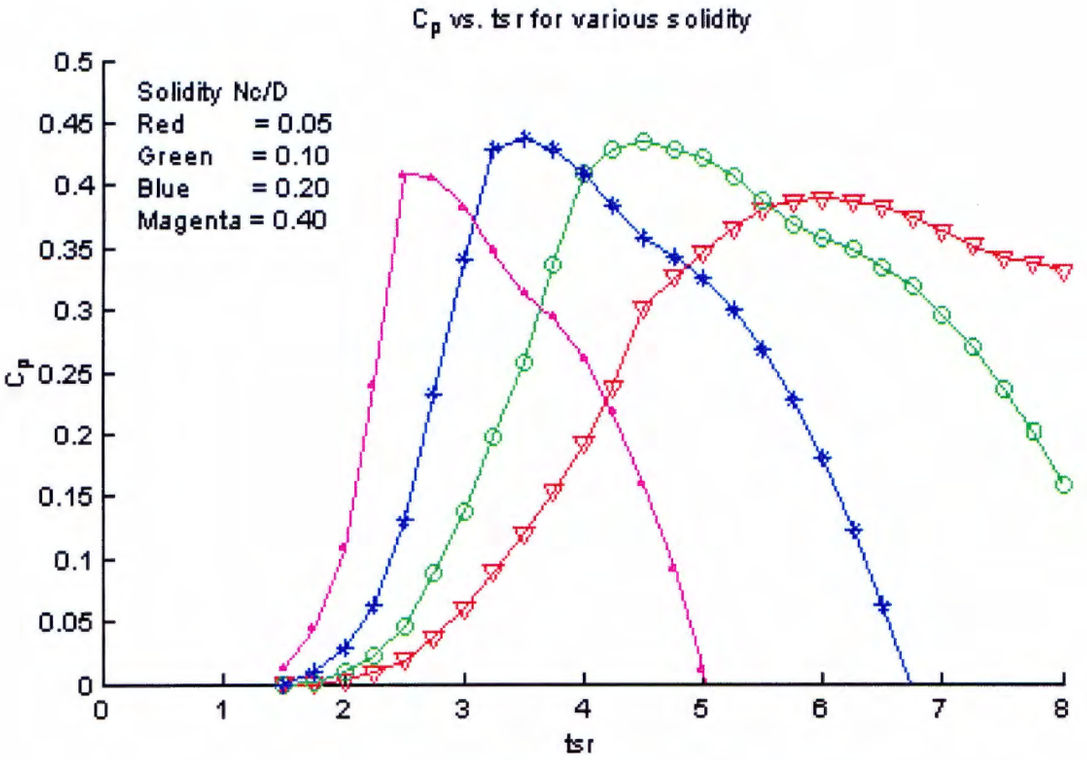

Figure 28: Diagram of Cp vs. TSR for various solidity

According to this diagram the most favourable graph of the best performance is the magenta line. Therefore the solidity S of 0.4 is chosen and lead to the following result:

$$S = \frac{N \cdot f}{2 \cdot R} \Rightarrow f = \frac{2 \cdot R \cdot S}{N} = \frac{2 \cdot 0{,}4m \cdot 0{,}4}{3}$$
$$f = 0{,}106667m = 10{,}6cm$$

To simplify later the construction process, the value 10 cm of the chord length f is chosen. Now all necessary values for the power calculation and then for the construction are determined.

3.4.3 *Torque and power calculation*

The next step is to put eqs. (23), (24) and (25) in the power equation in appendix II. To solve the overall power/torque calculation it is necessary to use Microsoft Excel, because especially with the eqs. (24) and (25) it is difficult to keep an overview. Because of this, appendix III shows the Excel calculation. The results are illustrated by the following values:
chord length f = 0,1 m, TSR λ = 4, blade length l = 0,8 m, radius R = 0,4 m, wind speed V_w = 6 m/s and induced wind velocity V_a = 5,31 m/s

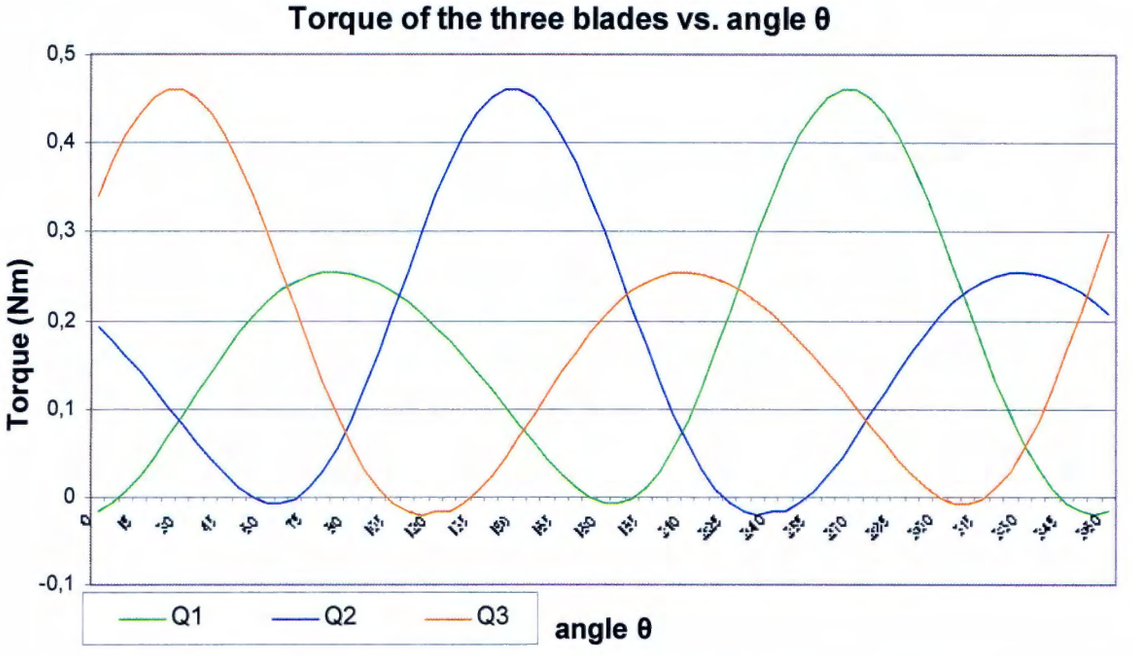

Figure 29: Torque of the three blades

It is seen that the fluctuation of the single torques of the three blades is enormous. This depends on the high impact of the angle of attack. In this case the difference between the two extremes of the total torque is approximately 0.5 Nm, which is shown finally in the graph power vs. angle θ.

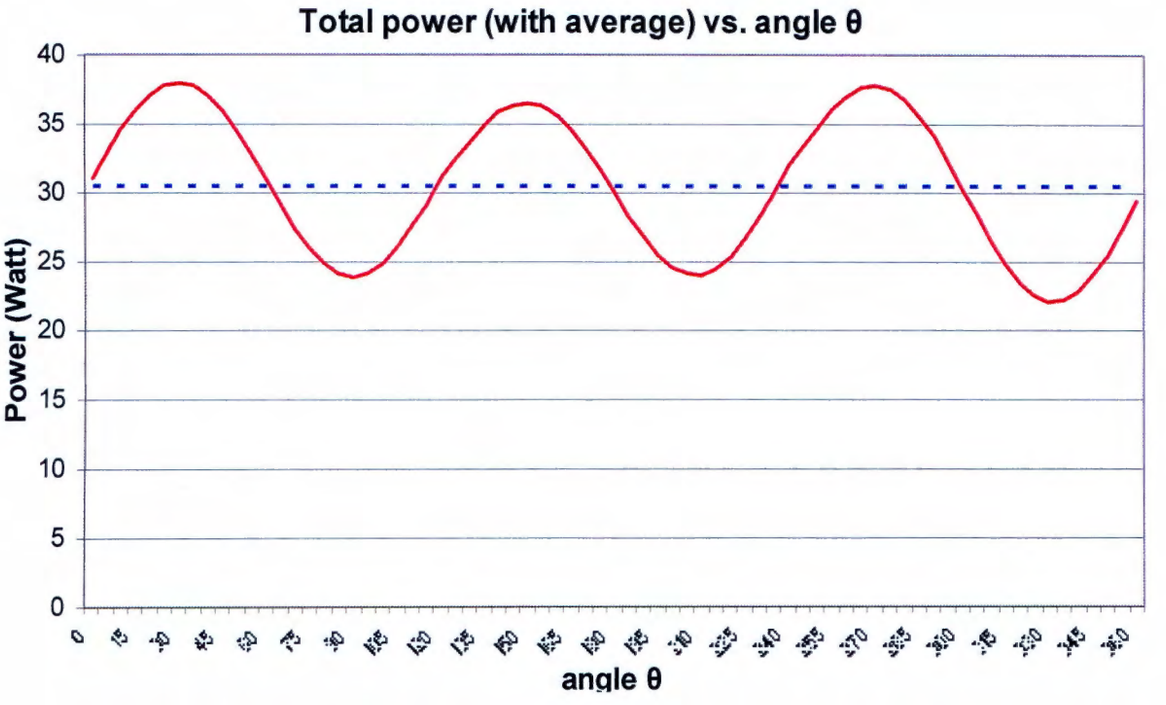

Figure 30: Calculated total power of the H-Rotor

The average power (blue line) with the selected values is more or less 30,5 Watt (also seen in appendix III), what is the guide value of the assembled H-Rotor.

With the given condition we can calculate with equation (6), the power available in the wind:

(5) in (6):

$$P_a = \frac{1}{2} \cdot \rho \cdot A \cdot V_w^{\ 3} = \frac{1}{2} \cdot \rho \cdot 2 \cdot R \cdot l \cdot V_w^{\ 3}$$

$$P_a = \frac{1}{2} \cdot 1{,}18 \frac{kg}{m^3} \cdot 2 \cdot 0{,}4m \cdot 0{,}8m \cdot \left(6 \frac{m}{s}\right)^3$$

$$P_a = 81{,}56W$$

The ratio between the theoretical and the available power of the H-Rotor can then be calculated as follows:

$$C_P = \frac{P}{P_a} \qquad (27)$$

$$C_P = \frac{P}{P_a} = \frac{30{,}5W}{81{,}56W}$$
$$C_P = 0{,}374 \Rightarrow 37{,}4\%$$

However, that's not the total power coefficient C_p because the mechanical and electrical losses of the generator are not included in this calculation.

3.4.4 *Torque/power with different TSR*

Furthermore with the help of Microsoft Excel the dependence of the torque/power from the Tip speed rate can be analysed. The following plots show the results.

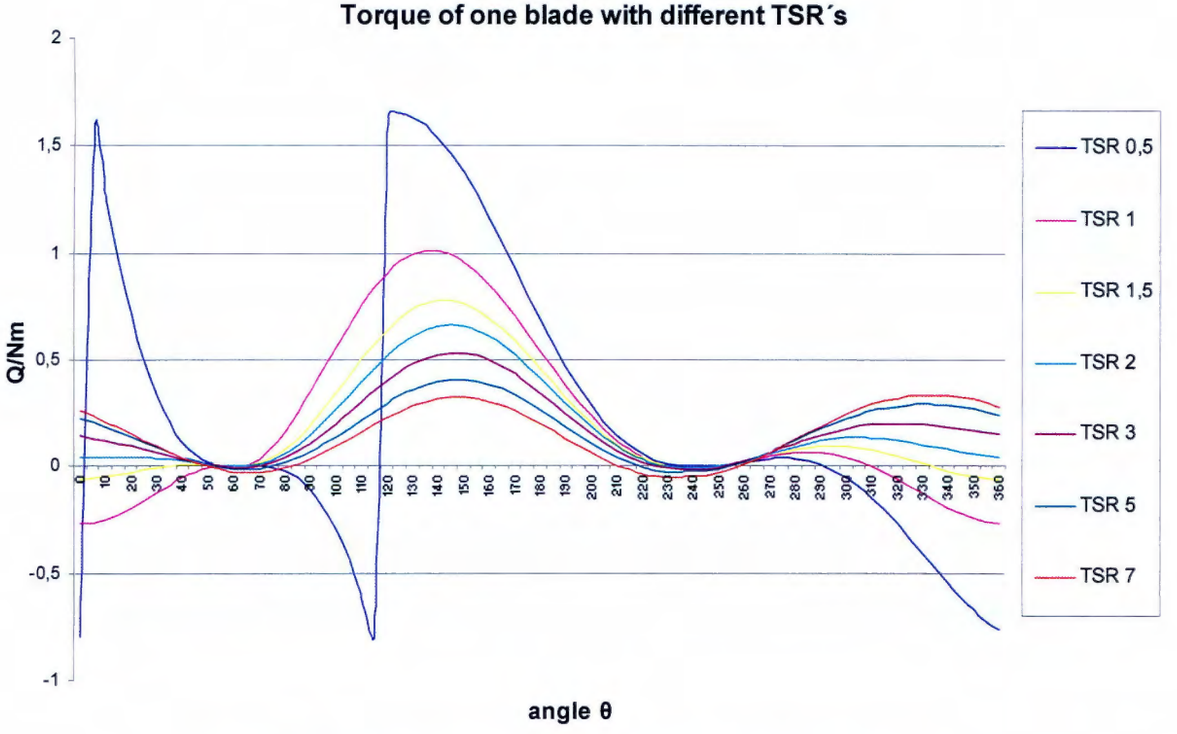

Figure 31: Diagram of the torque of one blade with different TSR

It is seen, that at TSR of 0.5 the torque has four extreme spikes in the positive and negative field. Considering that there are 3 blades in total, of course with 120 degrees dislocation, the H-Rotor runs very unevenly. But with increasing TSR there are only two extremes, which get lower and lower, and the run becomes more even. On the other hand the blade produces less torque by increasing TSR, because the blade speed V_t increases with the TSR.

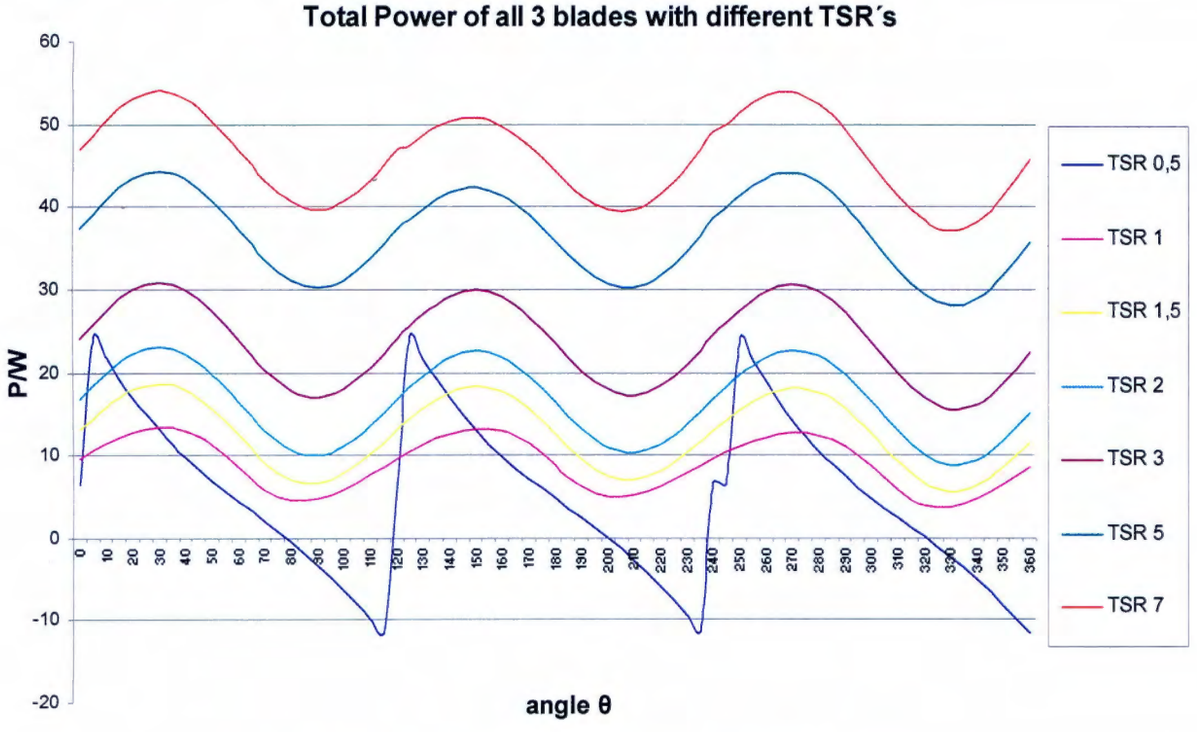

Figure 32: Diagram of the total power with different TSR

The diagram of the total power of the different TSR's shows that like in the figure before, the run by a TSR of 0.5 is very extreme, but the runs get more homogeneous with higher TSR. The runs have a form like waves and the difference of the two extremes is approximately 12 W. Unlike the diagram of the torque (Fig. 31) the power increases with higher TSR although the torque is falling. Considering in equation (1) that the wind velocity V_w is constant, means that the blade speed V_t is directly proportional to the TSR λ. This means that the

angular speed ω increases with higher TSR. Finally the part of ω on the power P (equation (20)) is decisively higher than the torque Q.

4.0 Construction process

Much attention must be paid so that the entire construction, which is made in ProEngineering, can easily be manufactured and assembled. For this, the construction is divided in 2 main parts, the "working" part (Part 1, like the blades with the support structure) and the "electrical" part (Part 2, mainly the generator with attachment and the shaft with bearing). Furthermore it is important to keep the costs as low as possible.

4.1 Determinations for the stress calculations

Firstly the highest possible loads are determined for the following calculations. The power available P_a in the wind is 81,56 W like already calculated in chapter 3.3.3 with the equation (8). Considering in the betz law in 2.1 only 59% of this power can theoretically be achieved.

$$P_{max} = 0{,}59 \cdot P_a = 0{,}59 \cdot 81{,}56W$$
$$P_{max} = 48{,}12W$$

According to equation (20) the lowest possible angular velocity ω is needed to get the highest torque Q. However ω depends on the tangential velocity of the blades V_t

$$\omega = \frac{V_t}{R} \tag{28}$$

and V_t in turn depends on the TSR λ (seen eq. (1)):

$$\lambda = \frac{V_t}{V_w} \Rightarrow V_t = \lambda \cdot V_w$$

As already mentioned the lowest ω is needed. This means that the lowest TSR λ has to be chosen (λ_{min} = 0,5). Therefore by putting (1) in (28), ω_{min} can be calculated:

$$\omega_{\min} = \frac{V_t}{R} = \frac{\lambda_{\min} \cdot V_w}{R} = \frac{0{,}5 \cdot 6\frac{m}{s}}{0{,}4m}$$

$$\omega_{\min} = 7{,}5\frac{1}{s}$$

After transposition eq. (20) the maximum torque Q can be investigated:

$$P = Q_{\max} \cdot \omega_{\min} \Rightarrow Q_{\max} = \frac{P_{\max}}{\omega_{\min}} = \frac{48{,}12W}{7{,}5\frac{m}{s}}$$

$$Q_{\max} = 6{,}416Nm$$

The last step is to calculate the maximum torque for one blade:

$$Q_{\max 1} = \frac{Q_{\max}}{3} = \frac{6{,}416Nm}{3}$$

$$Q_{\max 1} = 2{,}14Nm$$

4.2 Part 1

4.2.1 *Airfoil*

As is already mentioned, the airfoil type NACA 63 018 was chosen for the three blades. A profile of the airfoil is shown in the figure below.

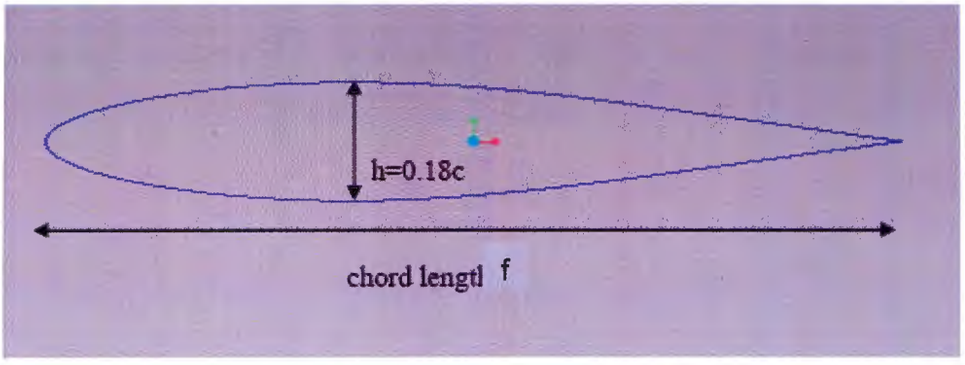

Figure 33: Profile of a NACA 63 018 airfoil

As the chord length f 100 mm has been chosen (see 3.3.2) what means that the thickness of the blade h is 18 mm. With this information and the coordinates of the program DesignFOIL (seen in Appendix IV) the profile can be designed in ProEngineering.

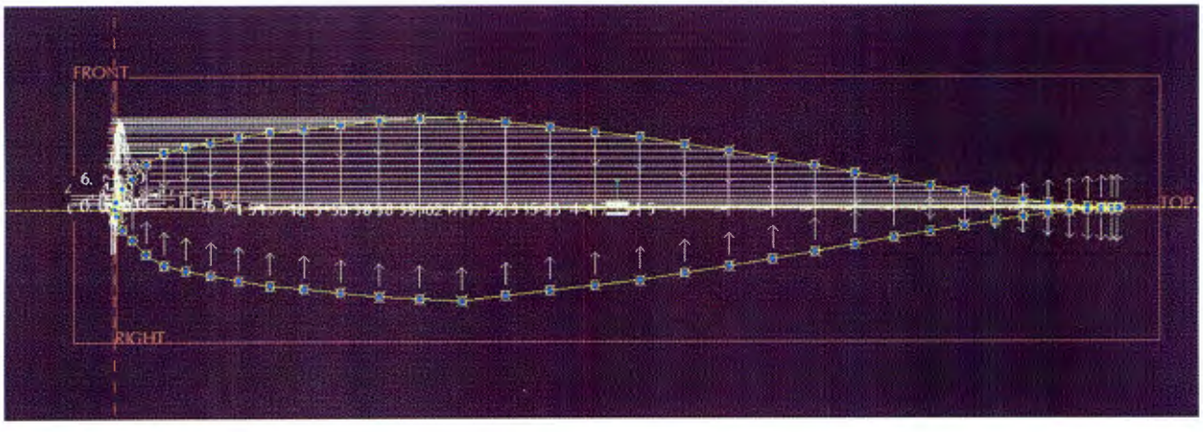

Figure 34: Construction of the airfoil profile in ProE

The most common material for the blades is extruded polystyrene (EPS) foam. But we chose wood as the material because it has lightweight properties and the costs can be reduced. A good wood type in this case is fir or spruce. Another import advantage is the manufacturability. The wood would come easily and can be quickly cut into the airfoil shape and with the using of an emery paper the surface would come out smooth without any roughness. It is additionally recommended to cover the blades with a special lacquer to protect them against rain or other atmospheric conditions. As already mentioned the length of the blade is 0.8 m. Additionally every blade has two milled depressions with two bore holes respectively (see Figure 36 and 37) to fix the support arms, however the holes have countersunk on the front side.

Figure 35: Front view of the airfoil

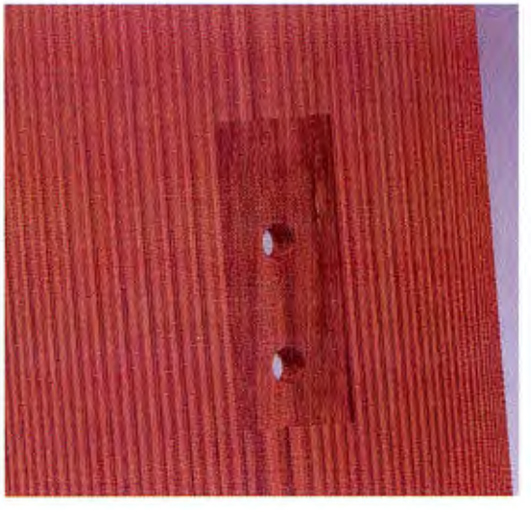

Figure 36: Back view of the airfoil

4.2.2 *Support arms*

As with the entire construction the importance of the support arms manufacturability and lightweight is imperative. This leads to the selection of aluminium (ENAW-AlMg3-H111) as main material, as it is lightweight, has a prescribed amount of rigidity and stress resistance and is low cost. Each blade has two bended support arms because the material aluminium is very flexible.

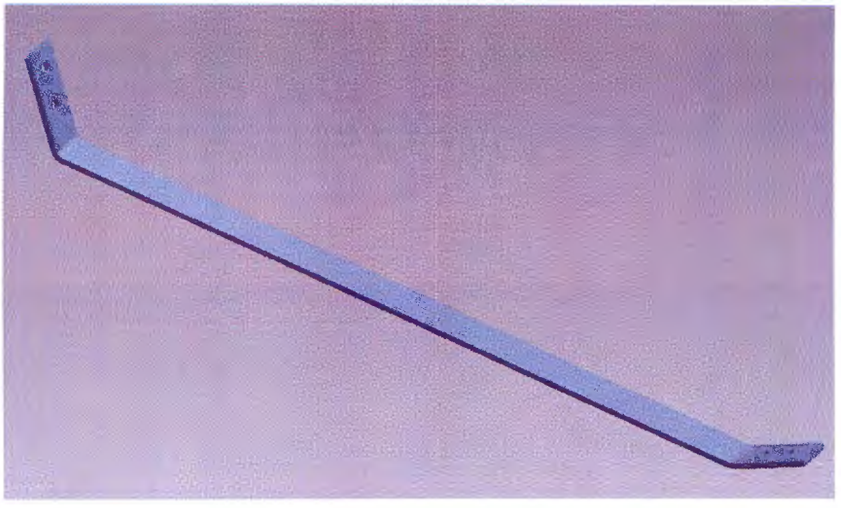

Figure 37: Aluminium support arm

The arms are fixed on the blades with a stabile screw-nut-connection however countersunk-screws are used for the fixture to reduce the wind resistance.

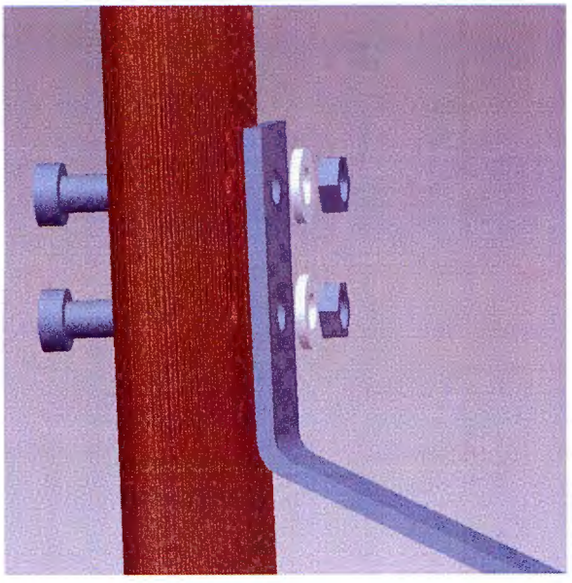

Figure 38: Assembly of blade and support arm

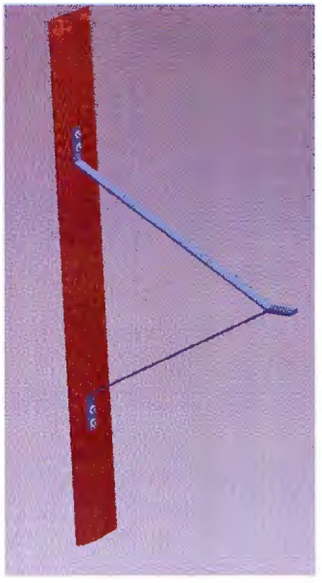

Figure 39: Blade with fixed support arms

To prove the stability of the support arms the following stress calculation is made:

Profile of the support arm

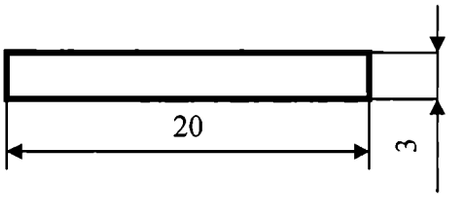

It is obvious that the support arm is stressed by bending, so the resisting moment for this kind of profile is called:

$$W_z = \frac{b^2 \cdot h}{6} \tag{29}$$

$$W_z = \frac{b^2 \cdot h}{6} = \frac{20^2 \cdot 3}{6} mm^3$$

$$W_z = 200mm^3$$

The maximum torque for one support arm is:

$$Q' = \frac{Q_{max1}}{2} = \frac{2{,}14 \cdot 10^3}{2} Nmm$$

$$Q' = 1070Nmm$$

And finally the maximum bending load is:

$$\sigma_{b\max} = \frac{Q'}{W_z} \tag{30}$$

$$\sigma_{b\max} = \frac{Q'}{W_z} = \frac{1070Nmm}{200mm^3}$$

$$\sigma_{b\max} = 5{,}35\frac{N}{mm^2} << \sigma_{b\,zul} = 70\frac{N}{mm^2}$$

This result shows that the bending load is clearly under the allowed limit.

4.2.3 *Turning platform*

The 3 blades with the support arms have to be fixed on the rotation axis to transfer the torque which is produced from the wind. For this two kinds of discs (also made of aluminium) are constructed, which are pressed together with screw connections. This turning platform is the connection between the support arms and the shaft or the connection between part 1 and 2.

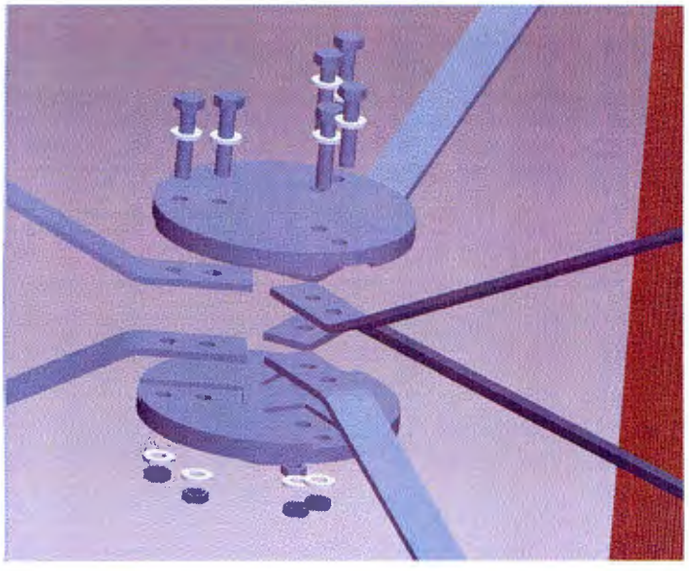

Figure 40: Fixation of the support arms on the two discs

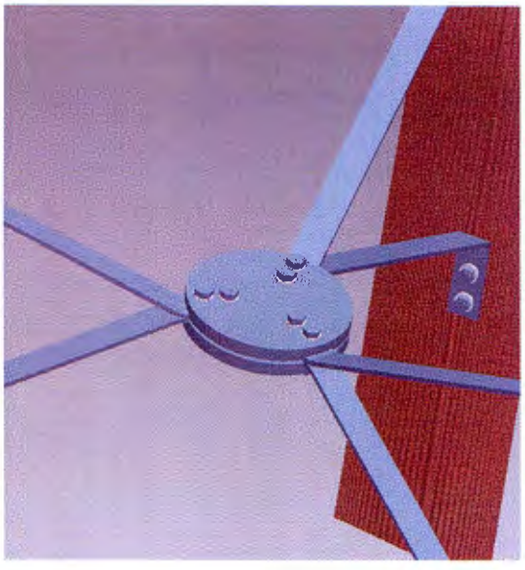

Figure 41: Assembled part 1

The two discs are almost equal expects the lower one, which is connected with the shaft. This one has a connecting piece with a borehole for the shaft. But both of them have three milled counterbores for the support arms and another additional six boreholes.

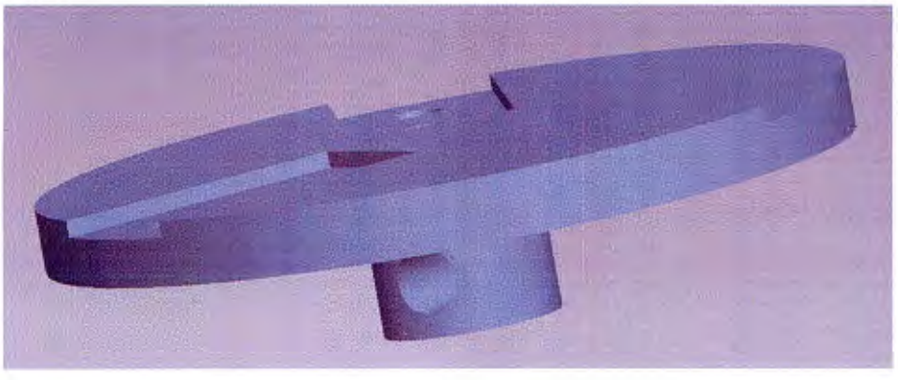

Figure 42: The lower disc of the turning table

4.3 Part 2

This part consists of the generator, the shaft, the bearing and the surrounded support structure. Also attached is the importance to make the manufacturing and the assembly simple. As the material for the shaft and the support structure is steel S235JR because some parts have to be welded which is very complicated with aluminium. It is correct that steel is heavier than aluminium, but isn't important because the weight now hasn't any influence on the function of the H-Rotor (not like the support arms).

4.3.1 *Generator System*

The final step in creating energy is to convert the mechanical energy of the turbine into usable electrical energy. One characteristic for the selected generator is to work with a power source (the wind turbine rotor) which supplies very fluctuating torques. Furthermore the intention of the entire wind turbine is to use it for experimental purposes what means it is sufficient to produce direct current (DC) and not alternating current (AC) for electricity network. Nearly all small commercial wind turbines use direct-drive permanent magnet generators, what means that is no gearbox necessary.

The motor as a generator

A lot of producers of small wind turbines were building their own generators which seemed a bit too complicated. The alternative is using a permanent magnet DC motor as a generator because the makeup is exactly the same only that now the rotor is driven mechanically. The rotor generates through the windings of the stator electrical energy. The permanent magnet DC motors are the simplest and most robust generator configuration and is nearly ideal for micro and mini wind turbines. They work as generators, but they weren't

designed to be generators, so they aren't great generators, but for our purpose it is satisfactory. Ideally you want the motor which generates the highest voltage for the least RPM. Last but not least the biggest advantage is that the motor function can overbear the starting torque, what is so high that most Darrieus H-Rotors cannot start by themself.

Generator selection

The generator has to fulfil some conditions:

- The minimum angular velocity ω_{min} = 7,5 U/s = 450 rpm (=U/min)
- The maximum angular velocity ω_{max} = 4500 rpm (see 4.1 with λ_{max}=5)
- The minimum transmitted torque Q_{min} = 0,6416 Nm (see 4.1)

The best apparently are a couple of models of motor made by Ametek. These models have the best properties and they are quite cheap. For this a 30 Volt DC Ametek PM motor is chosen (the information of the motor are shown in appendix V).

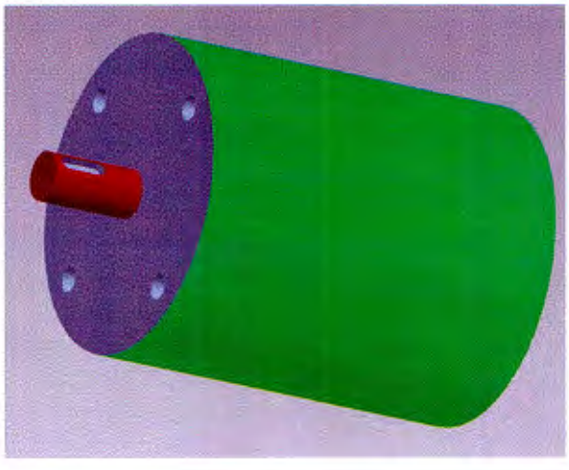

Figure 43: Simplified view in ProEngineering

4.3.2 *Shaft*

The next important part is the shaft, which connects part 1 with the generator. A hollow profile is chosen firstly to reduce weight and secondly to get the connection with the generator (Fig. 44) and turning platform (Fig. 42). Like already demonstrated in Fig. 44 the connection will be realized with a parallel key. Its rating depends on the measures of the hollow shaft, for this a calculation of the parallel key has to be done.

According to the Roloff/Matek book following equation is given:

$$D_a = 1{,}8 \cdot d \tag{31}$$

D_a: outer diameter, d: shaft diameter of the generator (d=16mm)

$$D_a = 1{,}8 \cdot d = 1{,}8 \cdot 16mm$$
$$D_a = 28{,}8mm$$

As the outer diameter D_a = 30 mm has been chosen. The inside diameter is D_i = 14 mm, because of the parallel key it has to be smaller than the shaft diameter d of the generator. The length of the hollow shaft is l_s = 300mm. Additionally it has to be machined on both sides because of the connections (Fig. 45 and 46).

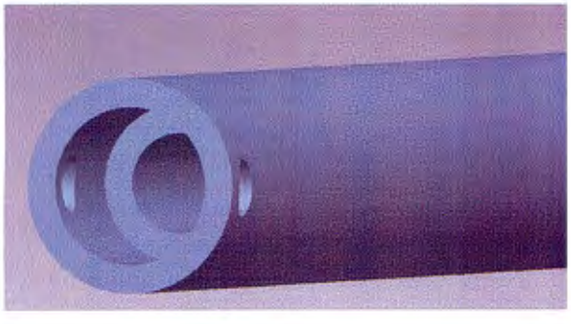

Figure 44: Connection point to the turning platform with threaded hole

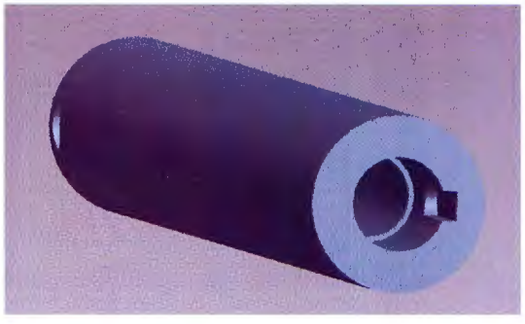

Figure 45: Connection point to the generator

4.3.3 *Parallel key*

The first part of the calculation is already done (see 4.3.2). With the given shaft diameter of the generator (d=16mm) the measurements of the parallel key can be made with the help of the Roloff/Matek table book (bxh = 5x5). Next we calculate the maximal stress and compare it with the allowed maximum stress.

Along with the last calculations, the equations of the Roloff/Matek book are used:

Medial surface pressure

$$p_m = \frac{2 \cdot K_A \cdot Q_{max} \cdot K_\lambda}{d \cdot h' \cdot l' \cdot n \cdot \varphi} \qquad (32)$$

K_A = 1,25 (Tb 3-5), Q_{max} = 6,42 Nm (4.1), K_λ = 1,5 (Tb 12-1), h' = 0,45xh (Tb 12-2), l' = l-b (l=16mm; Tb 12-2), n=1, φ = 1

$$p_m = \frac{2 \cdot K_A \cdot Q_{max} \cdot K_\lambda}{d \cdot h' \cdot l' \cdot n \cdot \varphi} = \frac{2 \cdot 1{,}25 \cdot 6{,}42 \cdot 10^3 \cdot 1{,}5}{16 \cdot 0{,}45 \cdot 5 \cdot (16-5) \cdot 1 \cdot 1}$$

$$p_m = 60{,}8 \frac{N}{mm^2}$$

Allowed maximum stress

$$p_{zul} = \frac{R_e}{S_F} \qquad (33)$$

R_e = 235N N/mm² (Tb1-1), S_F = 1,5 (Tb12-1b)

$$p_{zul} = \frac{R_e}{S_F} = \frac{235 \frac{N}{mm^2}}{1{,}5}$$

$$p_{zul} = 156{,}7 \frac{N}{mm^2}$$

The result shows that the parallel key can transmit the maximum torque. It is so constructed that the hollow shaft can be looped on the generator shaft after putting the parallel key in the prepared counterbore (see Fig. 47).

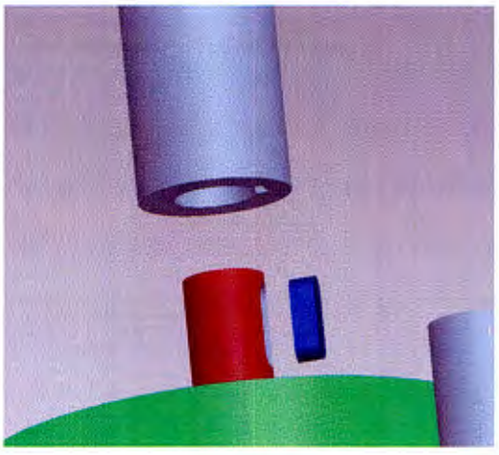

Figure 46: Assembly of hollow shaft, generator shaft and parallel key

4.3.4 *Bearing*

The bearing is used to facilitate the movement of shaft without using valuable mechanical energy. The bearing for the turbine must be able to withstand high speeds and must be able to rotate with great ease to reduce the amount of energy lost to the system. A stalling bearing could be the difference between 10 Watts of power and 20 Watts of power. The more energy the system uses to run, the less the output power will be.

A grooved ball bearing has been chosen because of its ability to run in high revolutions and furthermore the structure is simple and because of this the bearing is cheap. Moreover due to the better assembly properties we selected a flanged bearing from the manufacturer INA (type-nr.: RCJ30-N, see in appendix VI).

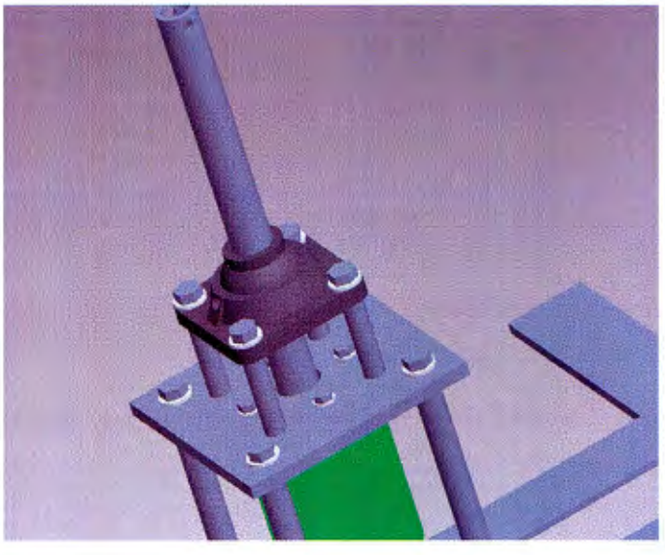

Figure 47: Assembled flanged bearing

4.3.5 *Support structure*

Finally to fix all the components of part 2 and also to stabilize the entire construction a robust support structure is needed, as well as ease of assembly. The constructed structure is a mixture of screw and welded connections. The material is again the common steel S235JR. The following pictures illustrate the entire support structure.

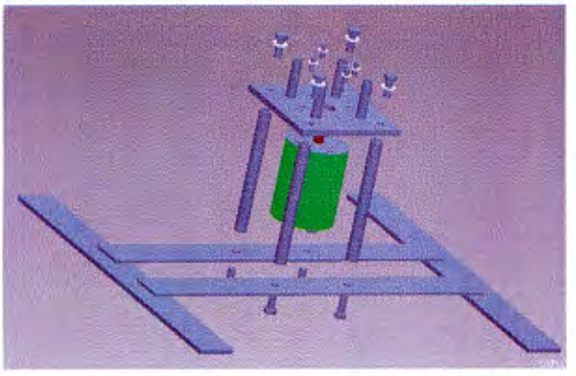

Figure 48: Exploded support structure of part 2

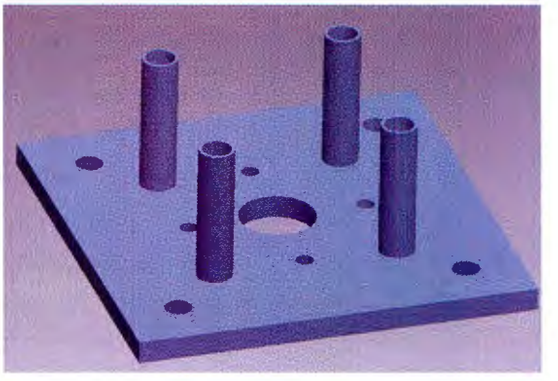

Figure 49: Mounting plate with 4 welded bars

4.4 Entire assembly

After completing construction of part 1 and 2 the entire assembly can be done. The connection between the two parts is made of a threaded pin (ISO 4766 DIN551), which is screwed in the prepared bore of the hollow shaft when the parts are connected (Fig. 51).

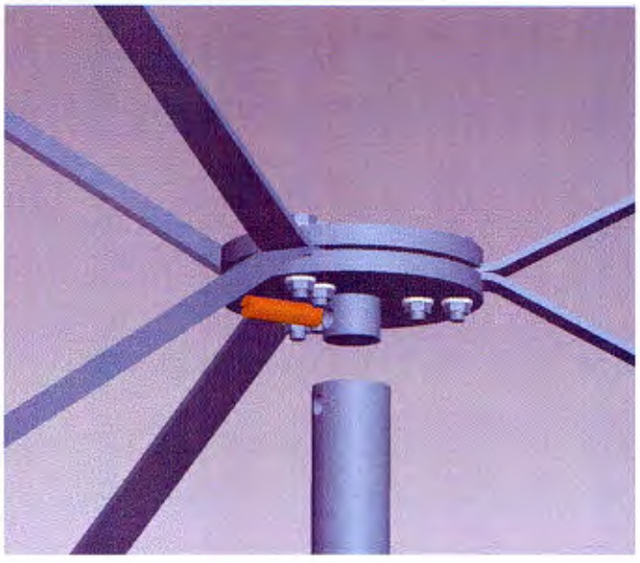

Figure 50: Assembly of part 1 and 2 with threaded pin

Next we will control if the pin is able to withstand the upcoming stresses. Furthermore it is obvious that it is stressed by the shearing strain.

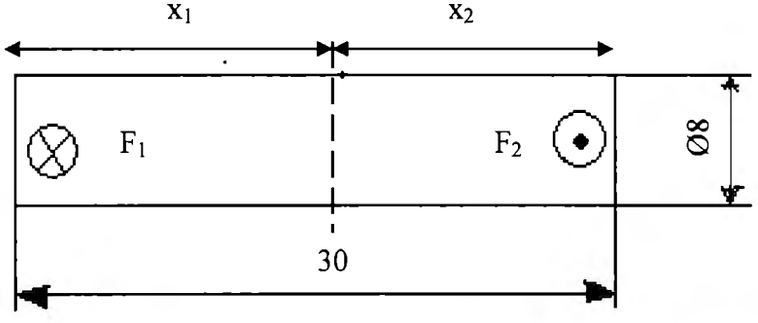

The maximal possible torque Q_{max} has to be divided. Then the loads on the certain points can be calculated:

$$Q_{1/2} = \frac{Q_{\max}}{2} = \frac{6{,}42Nm}{2}$$
$$Q_{1/2} = 3{,}21Nm$$
$$F_{1/2} = \frac{Q_{1/2)}}{x_{1/2}} = \frac{3{,}21 \cdot 10^3 Nmm}{15mm}$$
$$F_{1/2} = 214N$$

The maximum shearing strain can now be investigated:

$$\tau_{S\max} = \frac{F_{1/2}}{A} \qquad (34)$$
$$\tau_{S\max} = \frac{F_{1/2}}{A} = \frac{F_{1/2}}{\frac{1}{4}\pi \cdot d^2} = \frac{214N}{\frac{1}{4}\pi \cdot 8^2 mm^2}$$
$$\tau_{S\max} = 4{,}26\frac{N}{mm^2}$$

The material of a threaded pin is normally steel, where the lowest allowed shearing strain is by τ_{tSchN} = 160 N/mm² which is more than enough.

All the stress calculations showed that the H-Rotor would run without problem. The next picture demonstrates the assembly of the Darrieus turbine by ProEngineering (Fig. 52).

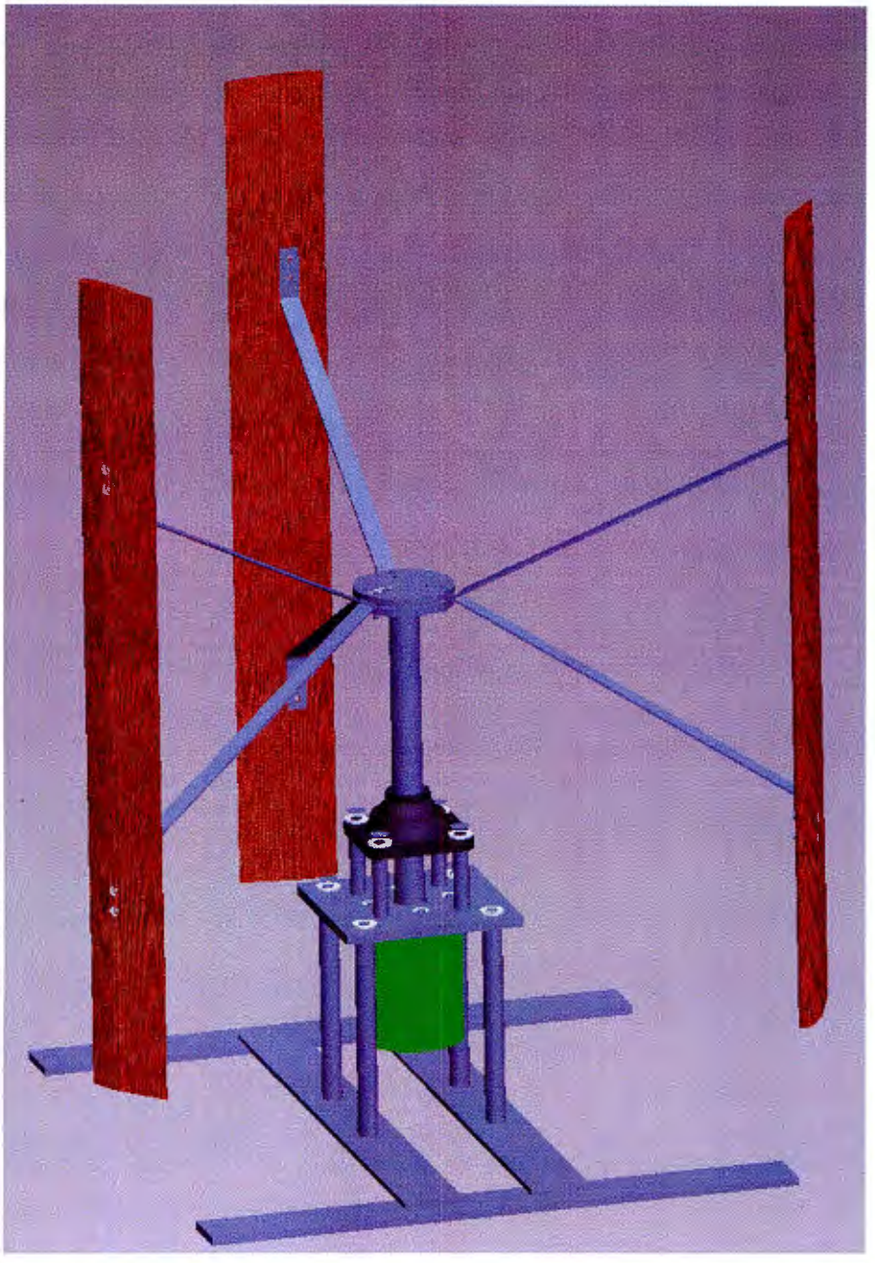

Figure 51: Assembly of the Darrieus H-Rotor

5.0 Performance testing

Testing is the only way to find the real performance (Cp curve) for all configurations of Darrieus wind turbine models. Tests could be also conducted in wind tunnel, but the cheapest and for this the favoured way is testing with multiple large fans.

5.1 Introduction – multiple fans test

The small straight bladed Darrieus wind turbine model (0.8m x 0.8m) can be tested using several large fans to obtain rough estimation of performance. The fan speed and number of fans could be varied during testing to study the changes of performance with wind speed and the influences of fan number.

The performance curve of a wind turbine can be measured in a number of ways. The most accurate way might be a generator/motor option by multiplying amperage and voltage, because in our model the generator is included. But there are other alternatives, like the classic method of friction brake. However, this method does not produce complete results under certain condition. A less well-known method is the angular acceleration of the rotor inertia mentioned in the Musgrove research paper. Equipment needed is minimal yet the method is capable of producing more complete result than the band brake method.

The performance trend with variation of wind speed can be analysed from these results. The effects of different number of fans to the model performance could be also discussed. Finally, the results from the band brake and the inertia acceleration method can be compared.

5.2 Setting up the rotor, the fans and the equipment

Positioning the fans and the rotor

The large fans can be lined side by side in the front of the rotor. Height of fans can be adjusted until their hubs are leveled with rotor's hub. The centre fan is pointed straight to the rotor centre while the two side fans are aimed slightly more toward the rotor instead of pointing straight forward so that the wind can reach the gap area between the fans. A thin stick with thread tied at one end can be used to roughly check the direction and strength of the wind at any point in front of the rotor.

Measuring the wind speed

Wind speed can be measured using a handheld propeller type anemometer. Instead of holding the anemometer directly, the meter is tied to one end of a thin stick to reduce obstruction by the reader's body. Wind speeds from 9 points in front of the rotor (swept area divided equally to 9 squares, speed taken at centre of each squares) can be collected and averaged. Prior to the measurement, the rotor blades stay stationary in an angular position where they do not obstruct the wind flow. Wind speeds at distance of 1.5 times radius from both sides of the rotor were can be also collected.

5.3 Band brake testing method

Setting up the band brake and the stroboscope

All the three airfoils are marked with the sign '-', 'x', and 'o' respectively at the centre to facilitate stroboscope measurement. The light of stroboscope is aimed toward the centre of rotor. If blade images with a single sign are captured by the stroboscope then the corresponding frequency is the rotor rpm. If the images' sign change at same pattern every time, in this case '-xo', then the corresponding frequency is 3 times the rpm.

The band brake, as shown in Figure 53, consists of a cotton rope with one end pulled by a spring scale while the other end is loaded with small weights. The cotton rope is tightened around the small pulley in the shaft. Rope type, rope contact angle, and pulley size can be adjusted to obtain the best reading from the brake.

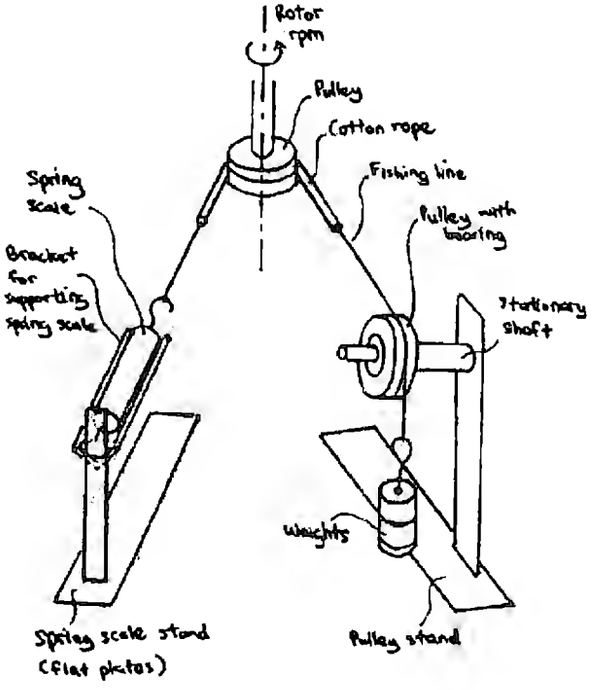

Figure 52: Band brake system

Measuring rotor torque from band brake

First, the rotor is accelerated to the maximum rpm in its unloaded condition. When the rpm stabilizes, the maximum rpm is obtained from the stroboscope. Next, small weights are added to the brake. The corresponding rpm and spring scale measurement are collected. The small weights are added until the rotor stalls. The time required to read the fluctuating rpm is long so the test is performed by 3 fans at 'High' speed condition only.

5.4 Inertia acceleration testing method

Setting up the tachometer and the reflective tape

The tachometer is positioned to emit the beam straight to the reflective tape so that the deflected beam will fall back on the tachometer. Cloth clipper is used to continuously press down the ON button. The timer is placed near the meter.

Recording the rpm changes from the tachometer

The rpm of the unloaded rotor is recorded from startup to maximum rpm for every 5 seconds interval. The test is performed under several fans with several different speed settings (high, medium, and low). Most of the time, the rotor is rotated to the highest torque position (one of the airfoils exactly parallel to the wind at counter wind half while the other two get pushed by wind at the wind assisted half) first before releasing it so that testing time can be reduced. Also, during the 'low' fan speed setting, the rotor remains at slow rotation refusing to accelerate up so the rotor has to be assisted by rotating the pulley using your hands until the acceleration pick up. The rpm is recorded only when the rotor acceleration starts to pick up. The test can be repeated with 2 fans and a single fan as well but using the maximum fan speed only.

6.0 Conclusion

As stated, the main goals of this project were twofold: to calculate and to construct a Darrieus wind turbine with H-rotor. The calculation gave a guide value of the theoretical power (P_a = 30,5 W) and the power coefficient (C_p = 37,4%), but only the praxis can confirm these values.

For this the realized construction in this thesis makes you able to build very easily the turbine because, like already mentioned, the costs for the components and the material are low and the fabrication is easy to handle.

Furthermore to test the performance some testing methods with multiple fans have been described. However firstly it is preferred to test with the attached generator to get the power and compare it to the theoretical power.

Finally the first step is done to build this H-rotor and to build up a laboratory for wind turbines.

Appendix I

Coordinates of C_d, C_f vs. AOA α of the airfoil type NACA 63-018 (Source: DesignFOIL) :

AOA α	Cl	Cd
-5	-0,388	0,0127
-4	-0,268	0,0121
-3	-0,148	0,0095
-2	-0,028	0,0093
-1	0,092	0,009
0	0,212	0,0093
1	0,332	0,0094
2	0,452	0,0094
3	0,572	0,01
4	0,692	0,0103
5	0,783	0,0142
6	0,862	0,0155
7	0,931	0,0167
8	0,991	0,0178
9	1,043	0,0189
10	1,086	0,022
11	1,12	0,0245
12	1,145	0,027
13	1,162	0,0298
14	1,171	0,0328
15	1,171	0,036
16	1,162	0,0292
17	1,145	0,0353
18	1,118	0,0407
19	1,081	0,0471
20	1,034	0,0533

Appendix II

Evaluation of the power equation:

eq. (9):

$$\tan\alpha = \frac{V_N}{V_C} \Rightarrow V_N = \tan\alpha \cdot V_C$$

(9) in (12):

$$W = \sqrt{V_C{}^2 + V_N{}^2} = \sqrt{V_C{}^2 + \tan^2\alpha \cdot V_C{}^2}$$

$$W = V_C \cdot \sqrt{1 + \tan^2\alpha}$$

(12) in (16):

$$F_l = C_l \frac{1}{2}\rho \cdot f \cdot l \cdot W^2$$

$$F_l = C_l \frac{1}{2}\rho \cdot f \cdot l \cdot V_C{}^2 \left(1 + \tan^2\alpha\right)$$

(14) in (16):

$$F_l = C_l \frac{1}{2}\rho \cdot f \cdot l \cdot V_C{}^2 \left(1 + \tan^2\alpha\right)$$

$$F_t = \left(C_l \sin\alpha - C_d \cos\alpha\right)\frac{1}{2}\rho \cdot f \cdot l \cdot V_C{}^2 \left(1 + \tan^2\alpha\right)$$

(7) in (16):

$$F_t = \left(C_l \sin\alpha - C_d \cos\alpha\right)\frac{1}{2}\rho \cdot f \cdot l \cdot V_C{}^2 \left(1 + \tan^2\alpha\right)$$

$$F_t = \left(C_l \sin\alpha - C_d \cos\alpha\right)\frac{1}{2}\rho \cdot f \cdot l \cdot \left(R\omega + V_a \cos\theta\right)^2 \left(1 + \tan^2\alpha\right)$$

(16) in (19), however for one blade:

$$Q = F_t \cdot R$$

$$Q = \frac{1}{2}\rho \cdot f \cdot l \cdot R \cdot \left(C_l \sin\alpha - C_d \cos\alpha\right) \cdot \left(R\omega + V_a \cos\theta\right)^2 \cdot \left(1 + \tan^2\alpha\right)$$

(19) in (20):

$$P = Q \cdot \omega$$

$$P = \frac{1}{2}\rho \cdot f \cdot l \cdot R\omega \cdot \left(C_l \sin\alpha - C_d \cos\alpha\right) \cdot \left(R\omega + V_a \cos\theta\right)^2 \cdot \left(1 + \tan^2\alpha\right)$$

(1) in (20):

$$\lambda = \frac{V_t}{V_w} = \frac{R\omega}{V_w} \Rightarrow R\omega = \lambda \cdot V_w$$

$$P = \frac{1}{2}\rho \cdot f \cdot l \cdot \lambda V_w \cdot \left(C_l \sin\alpha - C_d \cos\alpha\right) \cdot \left(\lambda V_w + V_a \cos\theta\right)^2 \cdot \left(1 + \tan^2\alpha\right)$$

5 variables

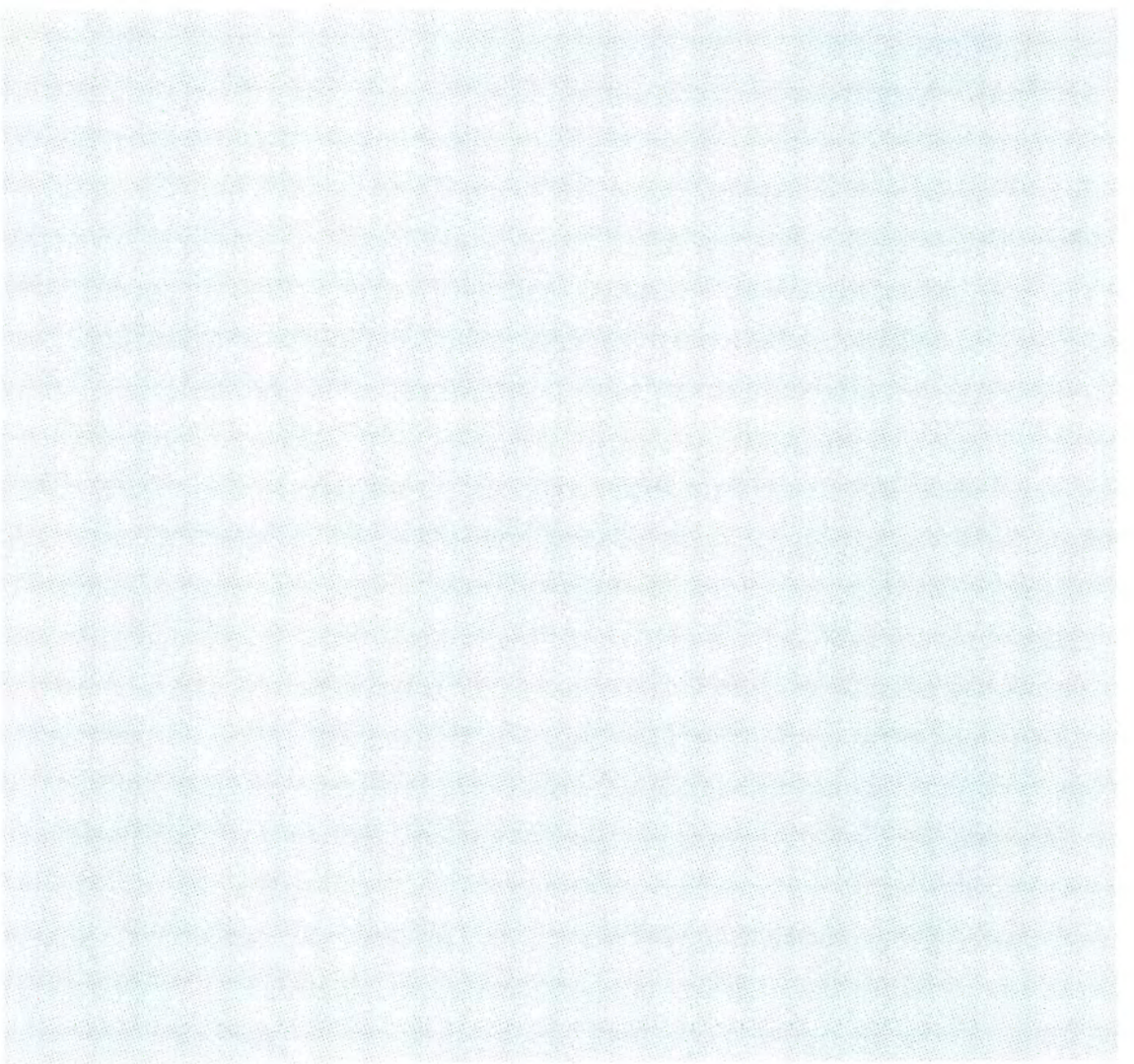

Appendix III

Microsoft Excel program for the power calculation:

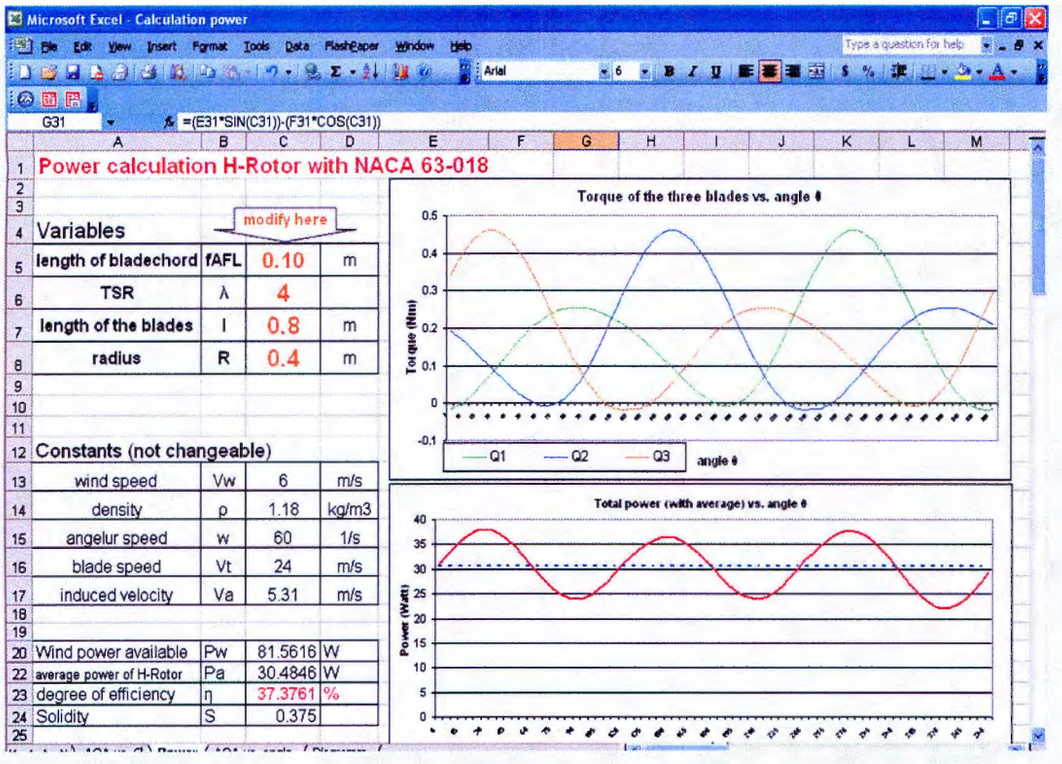

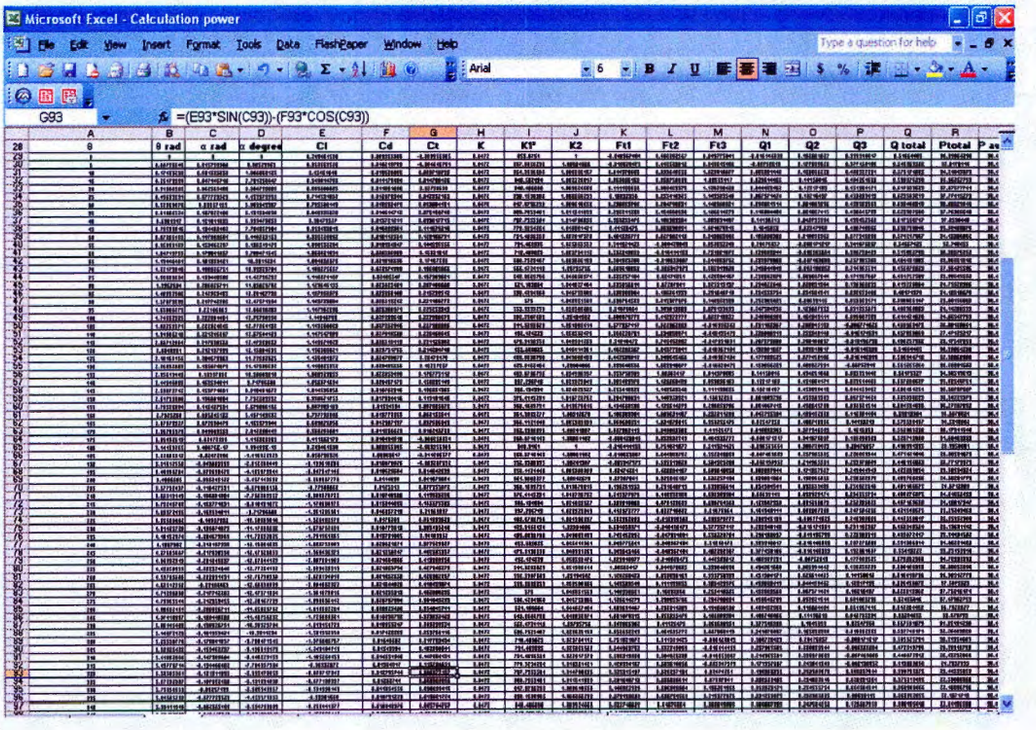

Appendix IV

Coordinates of NACA 63-018 from DesignFoil for the blade construction in ProE:

INDEX	X_Coord	Y_Coord	X_Coord*100mm	Y_Coord*18mm
1	1.000000	0.000000	100.000000	0
2	0.997987	0.000069	99.798715	0.013723331
3	0.991965	0.000313	99.196482	0.0626161
4	0.981981	0.000843	98.198146	0.168581121
5	0.968117	0.001820	96.811742	0.364020909
6	0.950484	0.003430	95.048445	0.686082663
7	0.929224	0.005847	92.922437	1.169384643
8	0.904508	0.009189	90.450847	1.837890223
9	0.876536	0.013447	87.653571	2.689324506
10	0.845531	0.018643	84.553134	3.728675097
11	0.811745	0.024720	81.174493	4.943942651
12	0.775449	0.031576	77.544850	6.315267086
13	0.736934	0.039044	73.693430	7.808730751
14	0.696513	0.046891	69.651252	9.378272295
15	0.654508	0.054837	65.450847	10.96736118
16	0.611260	0.062615	61.126047	12.52307147
17	0.567117	0.069933	56.711662	13.98665458
18	0.522432	0.076504	52.243239	15.30086696
19	0.477568	0.082042	47.756758	16.40835851
20	0.432883	0.086278	43.288338	17.25550592
21	0.388740	0.088993	38.873953	17.79853255
22	0.345491	0.090018	34.549150	18.00368726
23	0.303487	0.089266	30.348748	17.85317063
24	0.263066	0.087043	26.306567	17.40866154
25	0.224552	0.083509	22.455151	16.70185179
26	0.188255	0.078814	18.825510	15.76272249
27	0.154469	0.073112	15.446867	14.62242901
28	0.123464	0.066640	12.346426	13.32798451
29	0.095492	0.059425	9.549151	11.88500598
30	0.070776	0.051647	7.077561	10.3293106
31	0.049516	0.043420	4.951557	8.684089035
32	0.031883	0.035073	3.188257	7.014660537
33	0.018019	0.026633	1.801857	5.32656312
34	0.008035	0.017737	0.803521	3.547457978
35	0.002013	0.008963	0.201285	1.792655885
36	0.000000	0.000000	0.000000	0
37	0.002013	-0.008963	0.201285	-1.792655885
38	0.008035	-0.017737	0.803521	-3.547457978
39	0.018019	-0.026633	1.801857	-5.32656312
40	0.031883	-0.035073	3.188257	-7.014660537
41	0.049516	-0.043420	4.951557	-8.684089035

42	0.070776	-0.051647	7.077561	-10.3293106
43	0.095492	-0.059425	9.549151	-11.88500598
44	0.123464	-0.066640	12.346426	-13.32798451
45	0.154469	-0.073112	15.446867	-14.62242901
46	0.188255	-0.078814	18.825510	-15.76272249
47	0.224552	-0.083509	22.455151	-16.70185179
48	0.263066	-0.087043	26.306567	-17.40866154
49	0.303487	-0.089266	30.348748	-17.85317063
50	0.345491	-0.090018	34.549150	-18.00368726
51	0.388740	-0.088993	38.873953	-17.79853255
52	0.432883	-0.086278	43.288338	-17.25550592
53	0.477568	-0.082042	47.756758	-16.40835851
54	0.522432	-0.076504	52.243239	-15.30086696
55	0.567117	-0.069933	56.711662	-13.98665458
56	0.611260	-0.062615	61.126047	-12.52307147
57	0.654508	-0.054837	65.450847	-10.96736118
58	0.696513	-0.046891	69.651252	-9.378272295
59	0.736934	-0.039044	73.693430	-7.808730751
60	0.775449	-0.031576	77.544850	-6.315267086
61	0.811745	-0.024720	81.174493	-4.943942651
62	0.845531	-0.018643	84.553134	-3.728675097
63	0.876536	-0.013447	87.653571	-2.689324506
64	0.904508	-0.009189	90.450847	-1.837890223
65	0.929224	-0.005847	92.922437	-1.169384643
66	0.950484	-0.003430	95.048445	-0.686082663
67	0.968117	-0.001820	96.811742	-0.364020909
68	0.981981	-0.000843	98.198146	-0.168581121
69	0.991965	-0.000313	99.196482	-0.0626161
70	0.997987151	-6.86167E-05	99.798715	-0.013723331
71	1	0	100.000000	0

Appendix V

Motor data of Ametek 30 vdc generator:

AMETEK 30 VDC MOTOR / GENERATOR

Condition: Used Working
Voltage: 30 VDC Nominal
Diameter: 4"
Length: 5"
Shaft diameter: 5/8"
Shaft length" 1.25"
Mounting: 4 threaded holes on front
Leads: Black 12V White 12V Brown Ground
Ametek part number 116254

Makes a great wind or water wheel generator.
Pulled from working 1/2" reel to reel computer tape drive .

Guaranteed not DOA

Select a picture

Appendix VI

Bearing data:

Four-bolt flanged housing units

RCJ..-FA125

cast iron housing, radial insert ball bearing with eccentric locking collar, corrosion-resistant

The datasheet is only an overview of dimensions and basic load ratings for the selected series. Please ensure that you note all the guidance in these overview pages. Further information is given on many products under the menu item "Description". You can also obtain comprehensive information material via Catalogue selection (http://www.ina.de/content.ina.de/en/services/mediathek/library/library.jsp), by e-mail (kataloge@de.ina.com) or telephone +49 (91 32) 82 - 28 97.

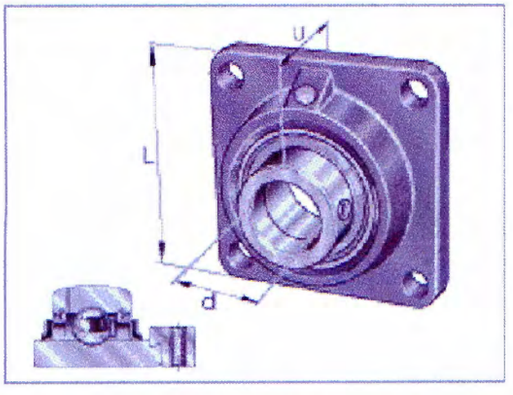

	d mm	L mm	U mm
RCJ20-N-FA125	20	86	45,6
RCJ25-N-FA125	25	95	45,9
RCJ30-N-FA125	30	108	50,1
RCJ35-N-FA125	35	118	53,3
RCJ40-N-FA125	40	130	58,9
RCJ45-FA125	45	137	58,9
RCJ50-N-FA125	50	143	66,1

Figure 1

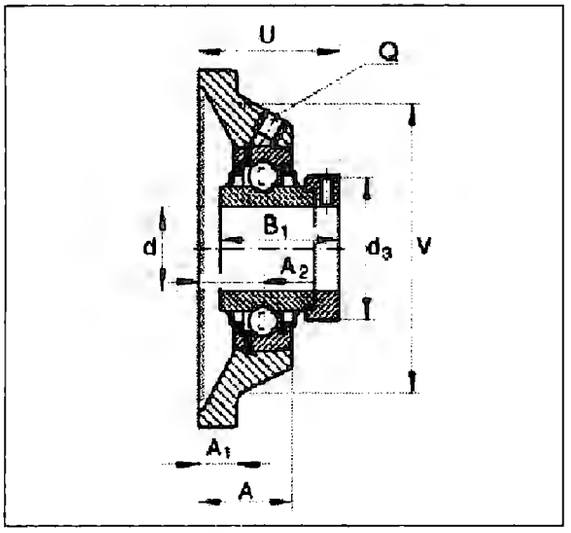

Figure 2

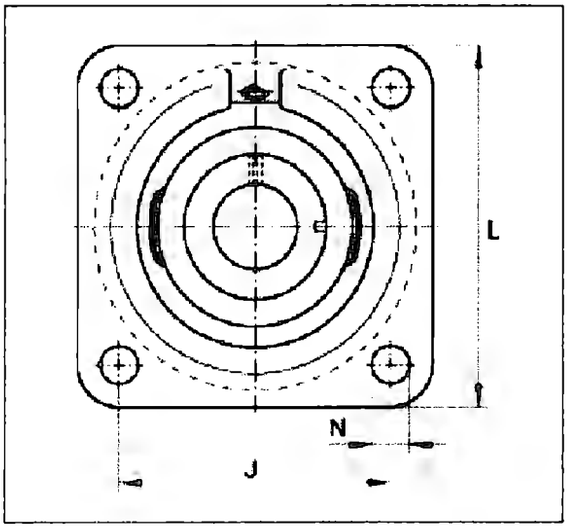

RCJ30-N-FA125

Figure 1 , Figure 2

d	30 mm	
L	108 mm	
U	50,1 mm	
A	29 mm	
A_1	12 mm	
A_2	20 mm	
B_1	48,5 mm	
$d_{3\,max}$	44 mm	
J	82,5 mm	
N	11,5 mm	
Q	Rp 1/8	
V	86 mm	
m	1,16 kg	Mass
Cr	19500 N	Basic dynamic load rating, radial
C_{0r}	11300 N	Basic static load rating, radial
GG CJ06-N-FA125.1		Designation of housing
GE30-KRR-B-FA125.5		Designation of bearing
KASK06		Bearing end cap To be ordered separately
		slot for bearing end cap

References

30 Volt DC Ametek PM motor, Ametek **http://www.ebay.com**

Betz criteria **http://en.wikipedia.org/wiki/Betz'_law**

Clean energy **http://www.ucsusa.org/clean_energy/renewable_energy_basics/how-wind-energy-works.html**

Darrieus Wind turbine analysis **http://www.windturbine-analysis.netfirms.com/**

Dieter Muhs, Herbert Wittel, Manfred Becker, Dieter Jannasch, Joachim Voßiek *Roloff/Matek Maschinenelemente, 16. Auflage*; Viewegs Fachbücher der Technik, July 2003

Dreese, John. DesignFOIL Software (TM). Dreese Code Software, **http://www.dreesecode.com/**.

EES Engineering Equation Solver **http://www.mhhe.com/engcs/mech/ees/**

Grooved ball bearing , INA-Schaeffler KG **http://www.ina.de**

Lift and drag **http://home.hccnet.nl/m.holst/LiftDrag.html**

Mazharul Islam, David S.-K. Ting, Amir Fartaj *Aerodynamic models for Darrieus-type straight-bladed vertical axis wind turbines*. Department of Mechanical, Automotive and Materials Engineering, University of Windsor, 2006

Primary energy distribution 2004
http://www.interacademycouncil.net/CMS/Reports/11840/11901/11905.aspx

Riegler H. HAWT versus VAWT: small VAWTs find a clear niche. Refocus 2003;4(4): 44-6

Tip speed ratio **http://en.wikipedia.org/wiki/Tip_speed_ratio**

Weibull-Distribution **http://en.wikipedia.org/wiki/Weibull_distribution**

Manwell JF, McGowan JG, Rogers AL. *Wind energy explained*; John Wiley & Sons Ltd: Amherst USA, 2002; 11, 60, 91, 145-152, 257

Poster

TECNOLÓGICO DE MONTERREY

GEORG SIMON OHM HOCHSCHULE NÜRNBERG

Construcción y Cálculo de un Darrieus Vertical Axis Wind Turbine con H-Rotor

Autor: Distler Johannes 1212107

Asesores:
Prof. Dr. Stütz (FH Nürnberg)
Dr. Ricardo Ganem
Dr. Jorge Eduardo Brieva

Problemática:

- La gasolina y la contaminación se han incrementado
- Desarrollo de energía renovable
- No existe mucha investigación de VAWT

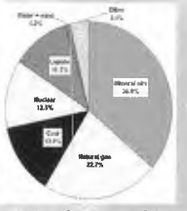

Figura 1: Distribución de energía primaria

Figura 2: Capacidad de energía del viendo

Objetivos:

- Cálculo de la turbina
- Construcción de una turbina Darrieus lisa
- Elaboración de un manual de funcionamiento para la utilización en un laboratorio especializado.

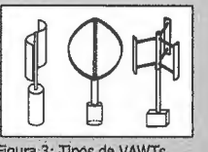

Figura 3: Tipos de VAWTs

El cálculo:

- Es complicado porque tiene muchos parametros
- El efecto depende mucho de la forma del airfoil
- Cada aspa tiene una fluctuación del torque del 0,45 Nm
- El efecto teórico es approximadamente 30 W
- El valor del coefficient del efecto C_p es 37,4%

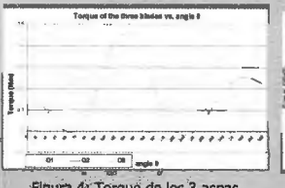

Figura 4: Torque de los 3 aspas

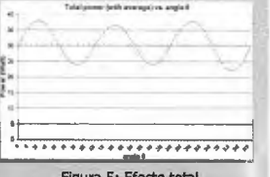

Figura 5: Efecto total

La construcción:

- Sencilla fabricación y ensamblaje
- dividido la construccion en dos partes para su transportación
- Material: aluminio

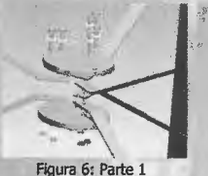

Figura 6: Parte 1

Figura 7: Parte 2

Conclusión:

- El cálculo se encuentra teóricamente correcto
- Los resultados del cálculo están bajo del criterio de Betz (59%)
- Se realizaron cálculos de esfuerzo en el prototipo.
- El costo de fabricación es bajo.

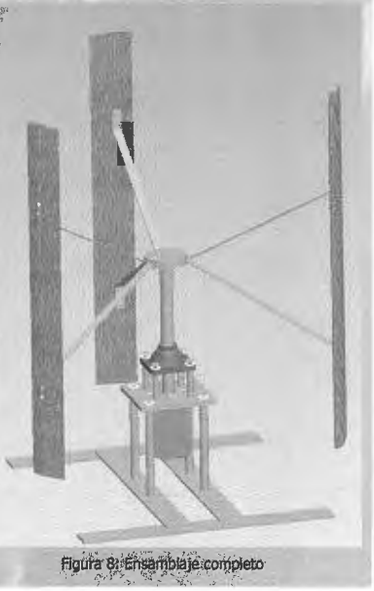

Figura 8: Ensamblaje completo